CHAPTER 3

Properties of GaN and ZnO Quantum Dots

Vladimir A. Fonoberov, Alexander A. Balandin

Nano-Device Laboratory, Department of Electrical Engineering, University of California–Riverside, Riverside, CA, USA

CONTENTS

1. INTRODUCTION

Gallium nitrite (GaN) and zinc oxide (ZnO) quantum dots (QDs) have recently attracted attention as promising nanostructures for optoelectronic, electronic, and spintronic applications. The band gap energy of GaN and ZnO is nearly the same (about 3.5 eV); however, the optical properties of GaN and ZnO QDs are different. Despite the growing interest to the GaN and ZnO QDs and progress in their synthesis, theoretical understanding of excitonic and phonon properties of GaN and ZnO QDs was lagging behind. This chapter aims at providing the first comprehensive description of excitonic and phonon properties of such QDs. The focus of the chapter is on theoretical description of the wurtzite and zincblende GaN QDs and wurtzite ZnO QDs. At the same time, whenever possible, we provide comparison of the theoretical results obtained for GaN and ZnO QDs with experimental data.

The chapter is divided into Section 2, which deals with GaN QDs, and Section 3, which is dedicated to ZnO QDs. Some of the technologically important topics reviewed in the chapter

ISBN: 1-58883-077-2

Handbook of Semiconductor Nanostructures and Nanodevices
Edited by A. A. Balandin and K. L. Wang
Volume 4: Pages (119–158)

include the effect of the AlN barrier on the GaN QD properties, the origin of ultraviolet (UV) photoluminescence (PL) in ZnO QDs, as well as optical phonon frequency shifts in ZnO QDs. The second half of the Section 3 discusses the interface and confined polar optical phonons in ZnO QDs, and provides details of our own experimental and theoretical study of Raman scattering from ZnO QDs. The chapter can be used as a reference source on the properties of a novel type of nanostructures such as GaN and ZnO QDs.

2. GaN QUANTUM DOTS

Recently, GaN QDs have attracted significant attention as promising candidates for application in optical, optoelectronic, and electronic devices. Progress in GaN technology has led to many reports on fabrication and characterization of different kinds of GaN QDs [1–8]. Molecular beam epitaxy growth in the Stranski-Krastanov mode of wurtzite (WZ) GaN/AlN [1, 2] and GaN/$Al_xGa_{1-x}N$ [3, 4] QDs has been reported. Other types of WZ GaN QDs have been fabricated by pulsed laser ablation of pure Ga metal in flowing N_2 gas [5], and by sequential ion implantation of Ga^+ and N^+ ions into dielectrics [6]. More recently, self-organized growth of zincblende (ZB) GaN/AlN QDs has been reported [7, 8].

Despite the large number of reports on the fabrication and optical characterization of WZ GaN/AlN and GaN/$Al_xGa_{1-x}N$ as well as ZB GaN/AlN QDs, there have been a small number of theoretical investigations of electronic states and excitonic properties of GaN QDs [9, 10]. Electronic states in WZ GaN/AlN QDs have been calculated in Ref. [9] using the plane wave expansion method. In addition to the restrictions imposed by any plane wave expansion method, such as the consideration of only 3D-periodic structures of coupled QDs and the requirement of a large number of plane waves for QDs with sharp boundaries, the model of Ref. [9] assumes equal elastic as well as dielectric constants for both the QD material and the matrix.

In this section, we follow our derivation given in Ref. [10] and present a theoretical model and numerical approach that allows one to accurately calculate excitonic and optical properties of strained GaN/$Al_xGa_{1-x}N$ QDs with WZ and ZB crystal structure. Using a combination of finite difference and finite element methods we accurately determine strain, piezoelectric, and Coulomb fields as well as electron and hole states in WZ GaN/AlN and GaN/$Al_xGa_{1-x}N$ as well as ZB GaN/AlN QDs. We take into account the difference in the elastic and dielectric constants for the QD and matrix (barrier) materials. We investigate in detail the properties of single GaN QDs of different shapes, such as a truncated hexagonal pyramid on a wetting layer for WZ GaN/AlN QDs [see Fig. 1(a)], a disk for WZ GaN/$Al_xGa_{1-x}N$ QDs, and a truncated square pyramid on a wetting layer for ZB GaN/AlN QDs [see Fig. 1(b)]. Our model allows direct comparison of excitonic properties of different types of GaN QDs with reported experimental data, as well as analysis of the functional dependence of these properties on QD size.

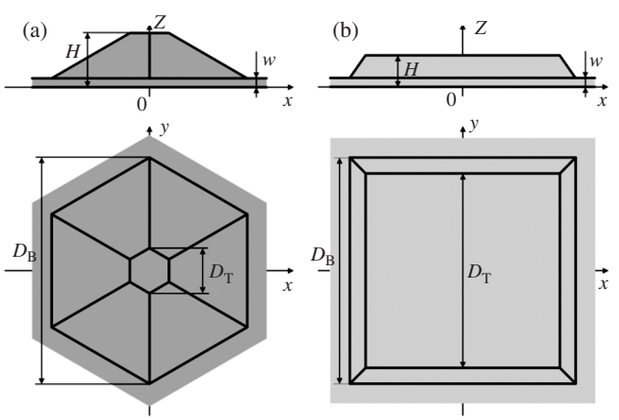

Figure 1. Schematic pictures of WZ GaN/AlN (a) and ZB GaN/AlN (b) QDs.

2.1. Electron and Hole States in Strained Wurtzite and Zincblende GaN Quantum Dots

Since GaN QDs are usually embedded in AlN matrix, we have to study the properties of GaN/AlN QDs. Structures consisting of several materials and containing QDs are called QD-heterostructures. Because of the abrupt change of material parameters at the interfaces of QD-heterostructures, there appears strain and piezoelectric fields in the heterostructure. Moreover, electron and hole states undergo a strong modification. To understand the physics inside the GaN/AlN QDs, we first have to develop a theory of electron and hole states in strained QD-heterostructures. Below we present such a theory and apply it to GaN/AlN QDs with both WZ and ZB crystal structures.

2.1.1. Strain Field in Quantum-Dot Heterostructures

The lattice constants in semiconductor heterostructures vary with coordinates. This fact leads to the appearance of the elastic energy [11]

$$F_{\text{elastic}} = \int_V d\mathbf{r} \sum_{ijlm} \frac{1}{2} \lambda_{ijlm}(\mathbf{r}) \varepsilon_{ij}(\mathbf{r}) \varepsilon_{lm}(\mathbf{r}), \tag{1}$$

where ε_{ij} is the strain tensor, λ_{ijlm} is the tensor of elastic moduli, V is the total volume of the system, and $ijlm$ run over the spatial coordinates x, y, and z. To account for the lattice mismatch, the strain tensor ε_{ij} is represented as [12]

$$\varepsilon_{ij}(\mathbf{r}) = \varepsilon_{ij}^{(\mathbf{u})}(\mathbf{r}) - \varepsilon_{ij}^{(0)}(\mathbf{r}), \tag{2}$$

where $\varepsilon_{ij}^{(0)}$ is the tensor of local intrinsic strain and $\varepsilon_{ij}^{(\mathbf{u})}$ is the local strain tensor defined by the displacement vector $\mathbf{u}$ as follows,

$$\varepsilon_{ij}^{(\mathbf{u})}(\mathbf{r}) = \frac{1}{2} \left(\frac{\partial u_i(\mathbf{r})}{\partial r_j} + \frac{\partial u_j(\mathbf{r})}{\partial r_i} \right). \tag{3}$$

To calculate the strain field [Eqs. (2), (3)] one has to find the displacement vector $\mathbf{u}(\mathbf{r})$ at each point of the system. This can be achieved by imposing boundary conditions for $\mathbf{u}(\mathbf{r}_\infty)$ at the endpoints $\mathbf{r}_\infty$ of the system and minimizing the elastic energy (1) with respect to $\mathbf{u}(\mathbf{r})$.

a. Zincblende Quantum Dots In crystals with ZB symmetry, there are only three linearly independent elastic constants: $\lambda_{xxxx} = C_{11}$, $\lambda_{xxyy} = C_{12}$, and $\lambda_{xyxy} = C_{44}$. Thus, the elastic energy (1) can be written as

$$F_{\text{elastic}} = \frac{1}{2} \int_V d\mathbf{r} (C_{11}(\varepsilon_{xx}^2 + \varepsilon_{yy}^2 + \varepsilon_{zz}^2) + 2C_{12}(\varepsilon_{xx}\varepsilon_{yy} + \varepsilon_{xx}\varepsilon_{zz} + \varepsilon_{yy}\varepsilon_{zz}) + 4C_{44}(\varepsilon_{xy}^2 + \varepsilon_{xz}^2 + \varepsilon_{yz}^2)). \tag{4}$$

Note that all variables under the sign of integral in Eq. (4) are functions of $\mathbf{r}$. For ZB QDs embedded into a ZB matrix with lattice constant a_{matrix}, the tensor of local intrinsic strain is

$$\varepsilon_{ij}^{(0)}(\mathbf{r}) = \delta_{ij}(a(\mathbf{r}) - a_{\text{matrix}})/a_{\text{matrix}}, \tag{5}$$

where $a(\mathbf{r})$ takes values of QD lattice constants inside QDs and is equal to a_{matrix} outside QDs.

b. Wurtzite Quantum Dots Following standard notation, it is assumed in the following that the z-axis is the axis of six-fold rotational symmetry in WZ materials. In crystals with WZ symmetry, there are five linearly independent elastic constants: $\lambda_{xxxx} = C_{11}$, $\lambda_{zzzz} = C_{33}$, $\lambda_{xxyy} = C_{12}$, $\lambda_{xxzz} = C_{13}$, and $\lambda_{xzxz} = C_{44}$. Thus, the elastic energy (1) can be written as

$$\begin{aligned} F_{\text{elastic}} = \frac{1}{2}\int_V d\mathbf{r}(C_{11}(\varepsilon_{xx}^2 + \varepsilon_{yy}^2) + C_{33}\varepsilon_{zz}^2 + 2C_{12}\varepsilon_{xx}\varepsilon_{yy} + 2C_{13}\varepsilon_{zz}(\varepsilon_{xx} + \varepsilon_{yy}) \\ + 4C_{44}(\varepsilon_{xz}^2 + \varepsilon_{yz}^2) + 2(C_{11} - C_{12})\varepsilon_{xy}^2), \end{aligned} \tag{6}$$

Note that all variables in the integrand of Eq. (6) are functions of $\mathbf{r}$. For WZ QDs embedded in a WZ matrix with lattice constants a_{matrix} and c_{matrix}, the tensor of local intrinsic strain is

$$\varepsilon_{ij}^{(0)}(\mathbf{r}) = (\delta_{ij} - \delta_{iz}\delta_{jz})(a(\mathbf{r}) - a_{\text{matrix}})/a_{\text{matrix}} + \delta_{iz}\delta_{jz}(c(\mathbf{r}) - c_{\text{matrix}})/c_{\text{matrix}}, \tag{7}$$

where $a(\mathbf{r})$ and $c(\mathbf{r})$ take values of the QD lattice constants inside the QDs and are equal to a_{matrix} and c_{matrix}, respectively, outside the QDs.

2.1.2. Piezoelectric Field in Quantum-Dot Heterostructures

Under an applied stress, some semiconductors develop an electric moment whose magnitude is proportional to the stress. The strain-induced polarization $\mathbf{P}^{\text{strain}}$ can be related to the strain tensor ε_{lm} using the piezoelectric coefficients e_{ilm} as follows:

$$\mathbf{P}_i^{\text{strain}}(\mathbf{r}) = \sum_{lm} e_{ilm}(\mathbf{r})\,\varepsilon_{lm}(\mathbf{r}), \tag{8}$$

where the indices ilm run over the spatial coordinates x, y, and z. Converting from tensor notation to matrix notation, Eq. (8) can be written as

$$\mathbf{P}_i^{\text{strain}}(\mathbf{r}) = \sum_{k=1}^{6} e_{ik}(\mathbf{r})\,\varepsilon_k(\mathbf{r}), \tag{9}$$

where

$$\{\varepsilon_{xx}, \varepsilon_{yy}, \varepsilon_{zz}, (\varepsilon_{yz}, \varepsilon_{zy}), (\varepsilon_{xz}, \varepsilon_{zx}), (\varepsilon_{xy}, \varepsilon_{yx})\} \equiv \{\varepsilon_1, \varepsilon_2, \varepsilon_3, \varepsilon_4, \varepsilon_5, \varepsilon_6\}$$

and

$$e_{ilm} = \begin{cases} e_{ik}, & k = 1, 2, 3 \\ \frac{1}{2}e_{ik}, & k = 4, 5, 6. \end{cases} \tag{10}$$

WZ nitrides also exhibit spontaneous polarization, $\mathbf{P}^{\text{spont}}$, with polarity specified by the terminating anion or cation at the surface. The total polarization,

$$\mathbf{P}(\mathbf{r}) = \mathbf{P}^{\text{strain}}(\mathbf{r}) + \mathbf{P}^{\text{spont}}(\mathbf{r}) \tag{11}$$

leads to the appearance of an electrostatic piezoelectric potential, V_p. In the absence of external charges, the piezoelectric potential is found by solving the Maxwell equation:

$$\nabla \cdot \mathbf{D}(\mathbf{r}) = 0 \tag{12}$$

where the displacement vector $\mathbf{D}$ in the system is

$$\mathbf{D}(\mathbf{r}) = -\hat{\varepsilon}_{\text{stat}}(\mathbf{r})\nabla V_p(\mathbf{r}) + 4\pi\mathbf{P}(\mathbf{r}). \tag{13}$$

In Eq. (13) $\hat{\varepsilon}_{\text{stat}}$ is the static dielectric tensor and $\mathbf{P}(\mathbf{r})$ is given by Eq. (11).

a. Zincblende Quantum Dots In crystals with ZB symmetry, only off-diagonal terms of the strain tensor give rise to the polarization. In component form,

$$\begin{aligned} P_x &= e_{14}\varepsilon_{yz}, \\ P_y &= e_{14}\varepsilon_{xz}, \\ P_z &= e_{14}\varepsilon_{xy}, \end{aligned} \tag{14}$$

where e_{14} is the only independent piezoelectric coefficient that survives, due to the ZB symmetry. The dielectric tensor in ZB materials reduces to a constant

$$\hat{\varepsilon}_{\text{stat}} = \begin{pmatrix} \varepsilon_{\text{stat}} & 0 & 0 \\ 0 & \varepsilon_{\text{stat}} & 0 \\ 0 & 0 & \varepsilon_{\text{stat}} \end{pmatrix}. \tag{15}$$

b. Wurtzite Quantum Dots Self-assembled WZ QDs usually grow along the z-axis. In this case, only the z-component of the spontaneous polarization is nonzero: $P_z^{\text{spont}} \equiv P_{\text{sp}}$, where P_{sp} is a specific constant for each material in a QD heterostructure. In crystals with WZ symmetry, the three distinct piezoelectric coefficients are e_{15}, e_{31}, and e_{33}. Thus, the polarization is given in component form by

$$\begin{aligned} P_x &= e_{15}\varepsilon_{xz}, \\ P_y &= e_{15}\varepsilon_{yz}, \\ P_z &= e_{31}(\varepsilon_{xx} + \varepsilon_{yy}) + e_{33}\varepsilon_{zz} + P_{\text{sp}}. \end{aligned} \tag{16}$$

As seen from Eq. (16), both diagonal and off-diagonal terms of the strain tensor generate a built-in field in WZ QDs. The dielectric tensor in WZ materials has the following form

$$\hat{\varepsilon}_{\text{stat}} = \begin{pmatrix} \varepsilon_{\text{stat}}^{\perp} & 0 & 0 \\ 0 & \varepsilon_{\text{stat}}^{\perp} & 0 \\ 0 & 0 & \varepsilon_{\text{stat}}^{\parallel} \end{pmatrix}. \tag{17}$$

2.1.3. Electron and Hole States in Strained Quantum-Dot Heterostructures

Since both GaN and AlN have large band gaps (see Ref. 10), we neglect coupling between the conduction and valence bands and consider separate one-band electron and six-band hole Hamiltonians. We also use proper operator ordering in the multi-band Hamiltonians, as is essential for an accurate description of QD heterostructures [13, 14].

Electron states are eigenstates of the one-band envelope-function equation:

$$\hat{H}_e \Psi_e = E_e \Psi_e, \tag{18}$$

where $\hat{H}_e$, Ψ_e, and E_e are the electron Hamiltonian, the envelope wave function and the energy, respectively. Each electron energy level is twofold degenerate with respect to spin. The two microscopic electron wave functions corresponding to an eigenenergy E_e are

$$\begin{cases} \psi_e = \Psi_e |S\rangle|\uparrow\rangle; \\ \psi_e = \Psi_e |S\rangle|\downarrow\rangle, \end{cases} \tag{19}$$

where $|S\rangle$ is Bloch function of the conduction band and $|\uparrow\rangle$, $|\downarrow\rangle$ are electron spin functions. The electron Hamiltonian $\hat{H}_e$ can be written as

$$\hat{H}_e = \hat{H}_S(\mathbf{r}_e) + H_e^{(\varepsilon)}(\mathbf{r}_e) + E_c(\mathbf{r}_e) + eV_p(\mathbf{r}_e), \tag{20}$$

where $\hat{H}_S$ is the kinetic part of the microscopic Hamiltonian unit-cell averaged by the Bloch function $|S\rangle$, $H_e^{(\varepsilon)}$ is the strain-dependent part of the electron Hamiltonian, E_c is the energy

of unstrained conduction band edge, e is the absolute value of electron charge, and V_p is the piezoelectric potential.

Hole states are eigenstates of the six-band envelope-function equation:

$$\hat{H}_h \Psi_h = E_h \Psi_h, \tag{21}$$

where $\hat{H}_h$ is 6×6 matrix of the hole Hamiltonian, Ψ_h is 6-component column of the hole envelope wave function, and E_h is the hole energy. The microscopic hole wave function corresponding to an eigenenergy E_h is

$$\psi_h = (|X\rangle|\uparrow\rangle,\ |Y\rangle|\uparrow\rangle,\ |Z\rangle|\uparrow\rangle,\ |X\rangle|\downarrow\rangle,\ |Y\rangle|\downarrow\rangle,\ |Z\rangle|\downarrow\rangle) \cdot \Psi_h, \tag{22}$$

where $|X\rangle$, $|Y\rangle$, and $|Z\rangle$ are Bloch function of the valence band and $|\uparrow\rangle$, $|\downarrow\rangle$ are spin functions of the missing electron. The hole Hamiltonian $\hat{H}_h$ can be written as

$$\hat{H}_h = \begin{pmatrix} \hat{H}_{XYZ}(\mathbf{r}_h) + H_h^{(\varepsilon)}(\mathbf{r}_h) & 0 \\ 0 & \hat{H}_{XYZ}(\mathbf{r}_h) + H_h^{(\varepsilon)}(\mathbf{r}_h) \end{pmatrix} + E_v(\mathbf{r}_h) + eV_p(\mathbf{r}_h) + H_{\mathrm{so}}(\mathbf{r}_h). \tag{23}$$

$\hat{H}_{XYZ}$ is a 3×3 matrix of the kinetic part of the microscopic Hamiltonian, unit-cell averaged by the Bloch functions $|X\rangle$, $|Y\rangle$, and $|Z\rangle$ (the crystal-field splitting is also included in $\hat{H}_{XYZ}$ for WZ QDs). $H_h^{(\varepsilon)}$ is a 3×3 matrix of the strain-dependent part of the hole Hamiltonian, E_v is the energy of the unstrained valence band edge, e is the absolute value of the electron charge and V_p is the piezoelectric potential. The last term in Eq. (23) is the Hamiltonian of spin-orbit interaction [13]:

$$H_{\mathrm{so}}(\mathbf{r}) = \frac{\Delta_{\mathrm{so}}(\mathbf{r})}{3} \begin{pmatrix} -1 & -i & 0 & 0 & 0 & 1 \\ i & -1 & 0 & 0 & 0 & -i \\ 0 & 0 & -1 & -1 & i & 0 \\ 0 & 0 & -1 & -1 & i & 0 \\ 0 & 0 & -i & -i & -1 & 0 \\ 1 & i & 0 & 0 & 0 & -1 \end{pmatrix}, \tag{24}$$

where Δ_{so} is the spin-orbit splitting energy.

a. Zincblende Quantum Dots For ZB QDs, the first term in the electron Hamiltonian (20) has the form

$$\hat{H}_S(\mathbf{r}) = \frac{\hbar^2}{2m_0} \hat{\mathbf{k}} \frac{1}{m_e(\mathbf{r})} \hat{\mathbf{k}}, \tag{25}$$

where $\hbar$ is Planck's constant, m_0 is the free-electron mass, $\hat{\mathbf{k}} = -i\nabla$ is the wave vector operator and m_e is the electron effective mass in units of m_0. The strain-dependent part of the electron Hamiltonian (20) is

$$H_e^{(\varepsilon)}(\mathbf{r}) = a_c(\mathbf{r})(\varepsilon_{xx}(\mathbf{r}) + \varepsilon_{yy}(\mathbf{r}) + \varepsilon_{zz}(\mathbf{r})), \tag{26}$$

where a_c is the conduction-band deformation potential and ε_{ij} is the strain tensor.

The matrix $\hat{H}_{XYZ}$ entering the hole Hamiltonian (23) is given by [13]

$$\hat{H}_{XYZ} = -\frac{\hbar^2}{2m_0} \begin{pmatrix} \hat{k}_x \beta_l \hat{k}_x + \hat{\mathbf{k}}_x^{\perp} \beta_h \hat{\mathbf{k}}_x^{\perp} & 3(\hat{k}_x \gamma_3^+ \hat{k}_y + \hat{k}_y \gamma_3^- \hat{k}_x) & 3(\hat{k}_x \gamma_3^+ \hat{k}_z + \hat{k}_z \gamma_3^- \hat{k}_x) \\ 3(\hat{k}_x \gamma_3^- \hat{k}_y + \hat{k}_y \gamma_3^+ \hat{k}_x) & \hat{k}_y \beta_l \hat{k}_y + \hat{\mathbf{k}}_y^{\perp} \beta_h \hat{\mathbf{k}}_y^{\perp} & 3(\hat{k}_y \gamma_3^+ \hat{k}_z + \hat{k}_z \gamma_3^- \hat{k}_y) \\ 3(\hat{k}_x \gamma_3^- \hat{k}_z + \hat{k}_z \gamma_3^+ \hat{k}_x) & 3(\hat{k}_y \gamma_3^- \hat{k}_z + \hat{k}_z \gamma_3^+ \hat{k}_y) & \hat{k}_z \beta_l \hat{k}_z + \hat{\mathbf{k}}_z^{\perp} \beta_h \hat{\mathbf{k}}_z^{\perp} \end{pmatrix}, \tag{27}$$

where $\hat{\mathbf{k}}_i^{\perp} = \hat{\mathbf{k}} - \hat{\mathbf{k}}_i$ $(i = x, y, z)$,

$$\begin{aligned} \beta_l &= \gamma_1 + 4\gamma_2, \\ \beta_h &= \gamma_1 - 2\gamma_2, \\ \gamma_3^{+} &= (2\gamma_2 + 6\gamma_3 - \gamma_1 - 1)/3, \\ \gamma_3^{-} &= (-2\gamma_2 + \gamma_1 + 1)/3. \end{aligned} \tag{28}$$

In Eq. (28), γ_1, γ_2, and γ_3 are the Luttinger-Kohn parameters of the valence band. The strain-dependent part, $H_h^{(\varepsilon)}$, of the hole Hamiltonian (23) can be written as [15]

$$H_h^{(\varepsilon)} = -a_v(\varepsilon_{xx} + \varepsilon_{yy} + \varepsilon_{zz}) + \begin{pmatrix} b(2\varepsilon_{xx} - \varepsilon_{yy} - \varepsilon_{zz}) & \sqrt{3}d\varepsilon_{xy} & \sqrt{3}d\varepsilon_{xz} \\ \sqrt{3}d\varepsilon_{xy} & b(2\varepsilon_{yy} - \varepsilon_{xx} - \varepsilon_{zz}) & \sqrt{3}d\varepsilon_{yz} \\ \sqrt{3}d\varepsilon_{xz} & \sqrt{3}d\varepsilon_{yz} & b(2\varepsilon_{zz} - \varepsilon_{xx} - \varepsilon_{yy}) \end{pmatrix}, \tag{29}$$

where a_v, b, and d are the hydrostatic and two shear valence-band deformation potentials, respectively. Note that all parameters in Eqs. (27) and (29) are coordinate-dependent for QD heterostructures.

b. Wurtzite Quantum Dots For WZ QDs, the first term in the electron Hamiltonian (20) has the form

$$\hat{H}_S(\mathbf{r}) = \frac{\hbar^2}{2m_0}\left(\hat{k}_z \frac{1}{m_e^{\parallel}(\mathbf{r})}\hat{k}_z + \hat{\mathbf{k}}_z^{\perp}\frac{1}{m_e^{\perp}(\mathbf{r})}\hat{\mathbf{k}}_z^{\perp}\right), \tag{30}$$

where $m_e^{\parallel}$ and $m_e^{\perp}$ are electron effective masses in units of m_0 and $\hat{\mathbf{k}}_z^{\perp} = \hat{\mathbf{k}} - \hat{\mathbf{k}}_z$. The strain-dependent part of the electron Hamiltonian (20) is

$$H_e^{(\varepsilon)}(\mathbf{r}) = a_c^{\parallel}(\mathbf{r})\varepsilon_{zz}(\mathbf{r}) + a_c^{\perp}(\mathbf{r})(\varepsilon_{xx}(\mathbf{r}) + \varepsilon_{yy}(\mathbf{r})), \tag{31}$$

where $a_c^{\parallel}$ and $a_c^{\perp}$ are conduction-band deformation potentials.

The matrix $\hat{H}_{XYZ}$ entering the hole Hamiltonian (23) is given by [14]

$$\hat{H}_{XYZ} = \frac{\hbar^2}{2m_0}\begin{pmatrix} \hat{k}_x L_1 \hat{k}_x + \hat{k}_y M_1 \hat{k}_y + \hat{k}_z M_2 \hat{k}_z & \hat{k}_x N_1 \hat{k}_y + \hat{k}_y N_1' \hat{k}_x & \hat{k}_x N_2 \hat{k}_z + \hat{k}_z N_2' \hat{k}_x \\ \hat{k}_y N_1 \hat{k}_x + \hat{k}_x N_1' \hat{k}_y & \hat{k}_x M_1 \hat{k}_x + \hat{k}_y L_1 \hat{k}_y + \hat{k}_z M_2 \hat{k}_z & \hat{k}_y N_2 \hat{k}_z + \hat{k}_z N_2' \hat{k}_y \\ \hat{k}_z N_2 \hat{k}_x + \hat{k}_x N_2' \hat{k}_z & \hat{k}_z N_2 \hat{k}_y + \hat{k}_y N_2' \hat{k}_z & \hat{k}_x M_3 \hat{k}_x + \hat{k}_y M_3 \hat{k}_y + \hat{k}_z L_2 \hat{k}_z - \delta_{\mathrm{cr}}, \end{pmatrix} \tag{32}$$

where

$$\begin{aligned} L_1 &= A_2 + A_4 + A_5, \\ L_2 &= A_1, \\ M_1 &= A_2 + A_4 - A_5, \\ M_2 &= A_1 + A_3, \\ M_3 &= A_2, \\ N_1 &= 3A_5 - (A_2 + A_4) + 1, \\ N_1' &= -A_5 + A_2 + A_4 - 1, \end{aligned}$$

$$N_2 = 1 - (A_1 + A_3) + \sqrt{2}A_6,$$
$$N_2' = A_1 + A_3 - 1,$$
$$\delta_{\rm cr} = 2m_0\Delta_{\rm cr}/\hbar^2. \tag{33}$$

In Eq. (33), A_k ($k = 1, \ldots, 6$) are Rashba-Sheka-Pikus parameters of the valence band and $\Delta_{\rm cr}$ is the crystal-field splitting energy. The strain-dependent part $H_h^{(\varepsilon)}$ of the hole Hamiltonian (23) can be written as [14]

$$H_h^{(\varepsilon)} = \begin{pmatrix} l_1\varepsilon_{xx} + m_1\varepsilon_{yy} + m_2\varepsilon_{zz} & n_1\varepsilon_{xy} & n_2\varepsilon_{xz} \\ n_1\varepsilon_{xy} & m_1\varepsilon_{xx} + l_1\varepsilon_{yy} + m_2\varepsilon_{zz} & n_2\varepsilon_{yz} \\ n_2\varepsilon_{xz} & n_2\varepsilon_{yz} & m_3(\varepsilon_{xx} + \varepsilon_{yy}) + l_2\varepsilon_{zz} \end{pmatrix}, \tag{34}$$

where

$$\begin{aligned} l_1 &= D_2 + D_4 + D_5, \\ l_2 &= D_1, \\ m_1 &= D_2 + D_4 - D_5, \\ m_2 &= D_1 + D_3, \\ m_3 &= D_2, \\ n_1 &= 2D_5, \\ n_2 &= \sqrt{2}D_6. \end{aligned} \tag{35}$$

In Eq. (35), D_k ($k = 1, \ldots, 6$) are valence-band deformation potentials. Note, that all parameters in Eqs. (32) and (34) are coordinate-dependent for QD heterostructures.

2.1.4. Results of Calculation and Discussion

The theory presented above is applied in this Section to describe excitonic properties of strained WZ and ZB GaN/AlN and WZ GaN/$Al_{0.15}Ga_{0.85}N$ QDs. We consider the following three kinds of single GaN QDs with variable QD height H: (i) WZ GaN/AlN QDs [see Fig. 1(a)] with the thickness of the wetting layer $w = 0.5$nm, QD bottom diameter $D_B = 5(H - w)$, and QD top diameter $D_T = H - w$ [1, 2]; (ii) ZB GaN/AlN QDs [see Fig. 1(b)] with $w = 0.5$ nm, QD bottom base length $D_B = 10(H - w)$, and QD top base length $D_T = 8.6(H - w)$ [7, 8]; (iii) Disk-shaped WZ GaN/$Al_{0.15}Ga_{0.85}N$ QDs with $w = 0$ and QD diameter $D = 3H$ [3, 4]. Material parameters used in our calculations are taken from Ref. 10. A linear interpolation is used to find the material parameters of WZ $Al_{0.15}Ga_{0.85}N$ from the material parameters of WZ GaN and WZ AlN.

It should be pointed out that WZ GaN/AlN and ZB GaN/AlN QDs are grown as 3-D arrays of GaN QDs in the AlN matrix [1, 2, 5, 6], while WZ GaN/$Al_xGa_{1-x}N$ QDs are grown as uncapped 2-D arrays of GaN QDs on the $Al_xGa_{1-x}N$ layer [3, 4]. While the distance between GaN QDs in a plane perpendicular to the growth direction is sufficiently large and should not influence optical properties of the system, the distance between GaN QDs along the growth direction can be made rather small. In the latter case, a vertical correlation is observed between GaN QDs, which can also affect optical properties of the system. The theory described above can be directly applied to describe vertically correlated WZ GaN/AlN and ZB GaN/AlN QDs. Since we are mainly interested in the properties of excitons in the ground and lowest excited states, here, we consider single GaN QDs in the AlN matrix. Within our model, uncapped GaN QDs on the $Al_xGa_{1-x}N$ layer can be considered as easily as GaN QDs in the $Al_xGa_{1-x}N$ matrix. In the following we consider GaN QDs in the $Al_xGa_{1-x}N$ matrix to facilitate comparison with WZ GaN/AlN and ZB GaN/AlN QDs.

The strain tensor in WZ and ZB GaN/AlN and WZ GaN/$Al_{0.15}Ga_{0.85}N$ QDs has been calculated by minimizing the elastic energy given by Eq. (4) for WZ QDs and the one given by Eq. (6) for ZB QDs with respect to the displacement vector $\mathbf{u}(\mathbf{r})$. We have carried

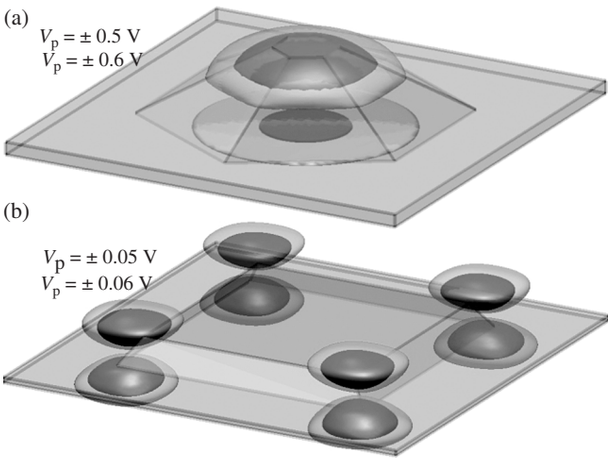

Figure 2. Piezoelectric potential in WZ GaN/AlN (a) and ZB GaN/AlN (b) QDs with height 3 nm.

out the numerical minimization of the elastic energy F_{elastic} by, first, employing the finite-element method to evaluate the integrals F_{elastic} as a function of $u_i(\mathbf{r_n})$, where $i = x, y, z$ and **n** numbers our finite-elements; second, transforming our extremum problem to a system of linear equations $\partial F_{\text{elastic}}/\partial u_i(\mathbf{r_n}) = 0$; and third, solving the obtained system of linear equations with the boundary conditions that $\mathbf{u}(\mathbf{r})$ vanishes sufficiently far from the QD.

Using the calculated strain tensor, we compute the piezoelectric potential for WZ and ZB GaN/AlN and WZ GaN/$Al_{0.15}Ga_{0.85}N$ QDs by solving the Maxwell equation [Eqs. (12), (13)] with the help of the finite-difference method. Figures 2(a) and 2(b) show the piezoelectric potential in WZ and ZB GaN/AlN QDs with height 3 nm, correspondingly. It is seen that the magnitude of the piezoelectric potential in a WZ GaN/AlN QD is about 10 times its magnitude in a ZB GaN/AlN QD. Moreover, the piezoelectric potential in the WZ QD has maxima near the QD top and bottom, while the maxima of the piezoelectric potential in the ZB QD lie outside the QD. The above facts explain why the piezoelectric field has a strong effect on the excitonic properties of WZ GaN/AlN QDs, while it has very little effect on those in ZB GaN/AlN QDs.

Both strain and piezoelectric fields modify bulk conduction and valence band edges of GaN QDs [see Eqs. (20) and (23)]. As seen from Figs. 3(a) and (b), the piezoelectric potential in a WZ GaN/AlN QD tilts conduction and valence band edges along the z-axis in such a way that it becomes energetically favorable for the electron to be located near the QD top and for the hole to be located in the wetting layer, near to the QD bottom. On the other hand, it is seen from Figs. 4(a) and (b) that the deformation potential in a ZB GaN/AlN QD

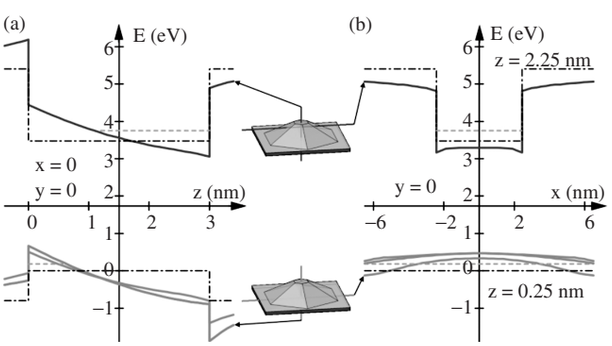

Figure 3. Conduction and valence band edges along z-axis (a) and along x-axis (b) for WZ GaN/AlN QD with height 3 nm (solid lines). The valence band edge is split due to the strain and crystal fields. Dash-dotted lines show the conduction and valence band edges in the absence of strain and piezoelectric fields. Dashed lines show positions of electron and hole ground state energies.

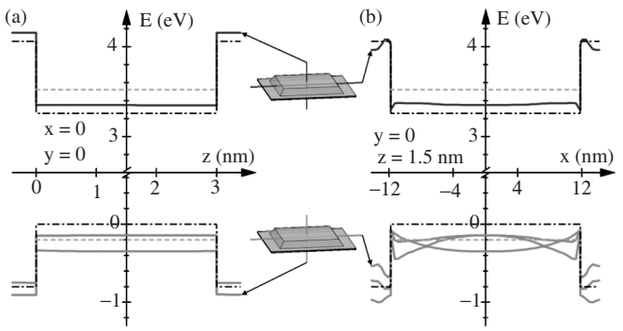

Figure 4. Conduction and valence band edges along z-axis (a) and along x-axis (b) for ZB GaN/AlN QD with height 3 nm (solid lines). The valence band edge is split due to the strain field. Dash-dotted lines show the conduction and valence band edges in the absence of strain field. Dashed lines show positions of electron and hole ground state energies.

bends the valence band edge in the xy-plane in such a way that it creates a parabolic-like potential well that expels the hole from the QD side edges. Figures 3 and 4 also show that the strain field pulls conduction and valence bands apart and significantly splits the valence band edge.

Using the strain tensor and piezoelectric potential, electron and hole states have been calculated following Section 2.1.3. We have used the finite-difference method similar to that of Ref. [16] to find the lowest eigenstates of the electron envelope-function equation (18) and the hole envelope-function equation (21). The spin-orbit splitting energy in GaN and AlN is very small (see Ref. 10); therefore, we follow the usual practice of neglecting it in the calculation of hole states in GaN QDs [9]. Figure 5 presents four lowest electron states in WZ and ZB GaN/AlN QDs with height 3 nm. Recalling the conduction band edge profiles (see Figures 2 and 3), it becomes clear why the electron in the WZ GaN/AlN QD is pushed to the QD top, while the electron in the ZB GaN/AlN QD is distributed over the entire QD. The behavior of the four lowest hole states in WZ and ZB GaN/AlN QDs with height 3 nm (see Fig. 6) can be also predicted by looking at the valence band edge profiles shown in Figs. 2 and 3. Namely, the hole in the WZ GaN/AlN QD is pushed into the wetting layer and is located near the QD bottom, while the hole in the ZB GaN/AlN QD is expelled from the QD side edges. Due to the symmetry of QDs considered in this chapter, the hole ground state energy is twofold degenerate, when the degeneracy by spin is not taken into account.

Both piezoelectric and strain fields are about seven times weaker in the WZ $GaN/Al_{0.15}Ga_{0.85}N$ QD than they are in the WZ GaN/AlN QD. Therefore, conduction and

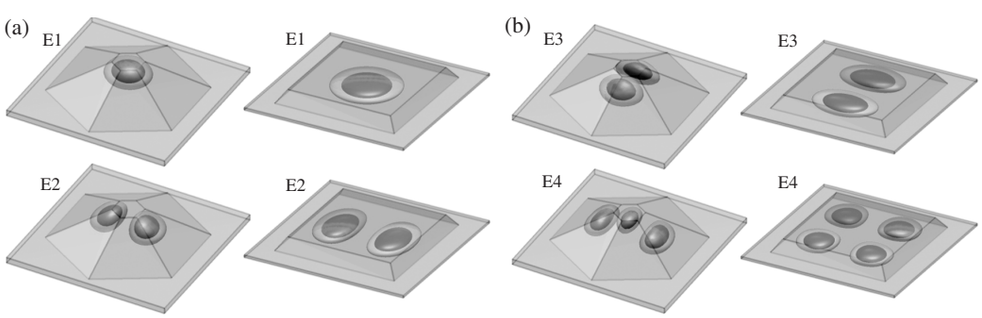

Figure 5. Isosurfaces of probability density $|\Psi|^2$ for the four lowest electron states in WZ GaN/AlN (left panel) and ZB GaN/AlN (right panel) QDs with height 3 nm. Outer (inner) isosurfaces contain 2/3 (1/3) of the total probability density. Energies of the electron states in the WZ QD are $E_1 = 3.752$ eV, $E_2 = 3.921$ eV, $E_3 = 3.962$ eV, and $E_4 = 4.074$ eV. Energies of the electron states in the ZB QD are $E_1 = 3.523$ eV, $E_2 = E_3 = 3.540$ eV, and $E_4 = 3.556$ eV.

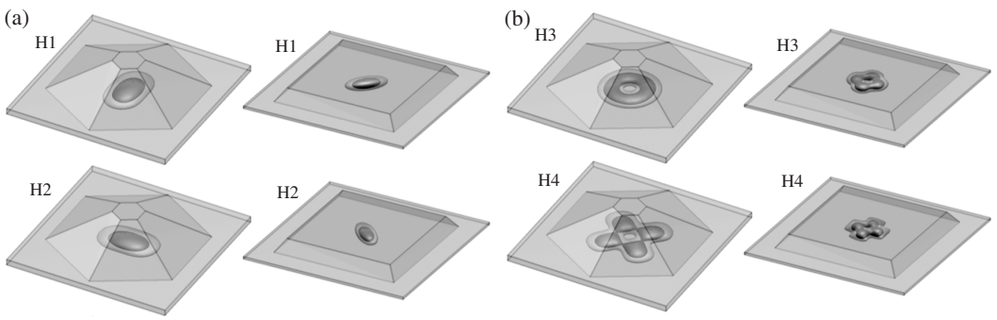

Figure 6. The same as in Fig. 5, but for the four lowest hole states. Energies of the hole states in the WZ QD are $E_1 = E_2 = 0.185$ eV, $E_3 = 0.171$ eV, and$E_4 = 0.156$ eV. Energies of the hole states in the ZB QD are $E_1 = E_2 = -0.202$ eV, $E_3 = -0.203$ eV, and $E_4 = -0.211$ eV.

valence band edges in WZ GaN/$Al_{0.15}Ga_{0.85}N$ QDs do not differ significantly from their bulk positions and the electron and hole states are governed mainly by quantum confinement.

Figure 7 shows electron and hole ground state energy levels in the three QDs. It is seen that the difference between the electron and hole energy levels decreases rapidly with increasing the QD height for WZ GaN/AlN QDs, unlike in two other kinds of QDs where the decrease is slower. The rapid decrease of the electron–hole energy difference for WZ GaN/AlN QDs is explained by the fact that the magnitude of the piezoelectric potential increases linearly with increasing the QD height.

Analyzing Figs. 8 and 9, one can notice two interesting effects. First, the increase of the QD size by a factor of two leads to a much smaller increase of the effective volume occupied by the electrons and holes. Second, for the depicted electron ground state and two first optically active hole states (for the incoming light polarized along the x-axis), the in-plane distribution of charge carriers in the ZB GaN/AlN QD resembles that in the WZ GaN/AlN QD if the coordinate system is rotated around the z-axis by $\pi/4$. Both phenomena can be explained by the effect of the strain field.

2.2. Optical Properties of GaN Quantum Dots

Now, when we have calculated electron and hole states in GaN QDs, we can proceed to the excitonic states and, therefore, to the optical properties of considered GaN/AlN QDs. However, first, we have to present a theory of electron–hole interaction in QD-heterostructures and discuss the calculation of oscillator strengths. Finally, this theory is applied to study the optical properties of WZ and ZB GaN/AlN QDs.

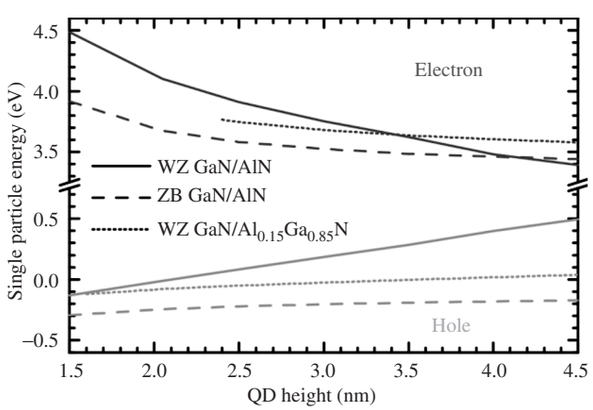

Figure 7. Electron and hole ground state energy levels as a function of QD height for three kinds of GaN QDs. Electron and hole energies in WZ GaN/$Al_{0.15}Ga_{0.85}N$ QDs are shown only for those QD heights that allow at least one discrete energy level.

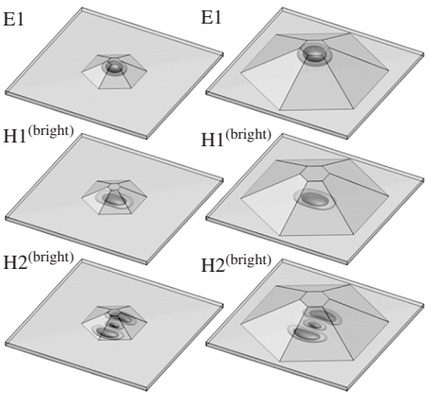

Figure 8. Isosurfaces of probability density $|\Psi|^2$ for the electron ground state, the hole ground state, and an excited hole state in WZ GaN/AlN QDs. Left-hand-side and right-hand-side panels correspond to QDs with height 2 nm and 4 nm, respectively. Outer (inner) isosurfaces contain 2/3 (1/3) of the total probability density.

2.2.1. Coulomb Potential Energy in Quantum-Dot Heterostructures

The Coulomb potential energy of the electron–hole system in a QD heterostructure is [16]

$$U(\mathbf{r}_e, \mathbf{r}_h) = U_{\text{int}}(\mathbf{r}_e, \mathbf{r}_h) + U_{s-a}(\mathbf{r}_e) + U_{s-a}(\mathbf{r}_h). \tag{36}$$

In Eq. (36), $U_{\text{int}}(\mathbf{r}_e, \mathbf{r}_h)$ is the electron–hole interaction energy, which is the solution of the Poisson equation:

$$\nabla_{\mathbf{r}_h}(\varepsilon_{\text{opt}}(\mathbf{r}_h)\nabla_{\mathbf{r}_h} U_{\text{int}}(\mathbf{r}_e, \mathbf{r}_h)) = \frac{e^2}{\varepsilon_0}\delta(\mathbf{r}_e - \mathbf{r}_h), \tag{37}$$

where ε_{opt} is the optical dielectric constant, ε_0 is the permittivity of free space, and δ is the Dirac delta function. The second and third terms on the right-hand side of Eq. (36) are the electron and hole self-interaction energies, defined as

$$U_{s-a}(\mathbf{r}) = -\frac{1}{2}\lim_{\mathbf{r}'\to\mathbf{r}}[U_{\text{int}}(\mathbf{r}, \mathbf{r}') - U_{\text{int}}^{\text{bulk}}(\mathbf{r}, \mathbf{r}')], \tag{38}$$

where $U_{\text{int}}^{\text{bulk}}(\mathbf{r}, \mathbf{r}')$ is the local bulk solution of Eq. (37), that is,

$$U_{\text{int}}^{\text{bulk}}(\mathbf{r}, \mathbf{r}') = -\frac{e^2}{4\pi\varepsilon_0\varepsilon_{\text{opt}}(\mathbf{r})|\mathbf{r} - \mathbf{r}'|}. \tag{39}$$

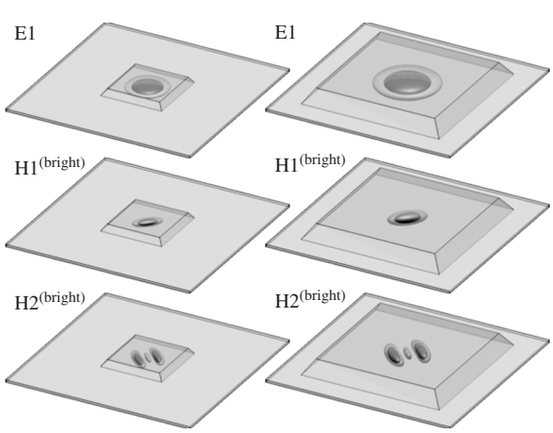

Figure 9. The same as in Fig. 8, but for ZB GaN/AlN QDs.

It should be pointed out that an infinite discontinuity in the self-interaction energy (38) arises at the boundaries between different materials of the heterostructure, when the optical dielectric constant $\varepsilon_{\text{opt}}(\mathbf{r})$ changes abruptly form its value in one material to its value in the adjacent material. This theoretical difficulty can be overcome easily by considering a transitional layer between the two materials, where $\varepsilon_{\text{opt}}(\mathbf{r})$ changes gradually between its values in different materials. The thickness of the transitional layer in self-assembled QDs depends on the growth parameters and is usually of order of one monolayer.

2.2.2. Exciton States, Oscillator Strengths and Radiative Decay Times

In the strong confinement regime, the exciton wave function ψ_{exc} can be approximated by the wave function of the electron–hole pair:

$$\psi_{\text{exc}}(\mathbf{r}_e, \mathbf{r}_h) = \psi_e^*(\mathbf{r}_e)\, \psi_h(\mathbf{r}_h), \tag{40}$$

and the exciton energy E_{exc} can be calculated considering the Coulomb potential energy (36) as a perturbation:

$$E_{\text{exc}} = E_e - E_h + \int_V d\mathbf{r}_e \int_V d\mathbf{r}_h U(\mathbf{r}_e, \mathbf{r}_h) |\psi_{\text{exc}}(\mathbf{r}_e, \mathbf{r}_h)|^2. \tag{41}$$

The electron and hole wave functions ψ_e and ψ_h in Eq. (40) are given by Eqs. (19) and (22), correspondingly. In Eq. (41), E_e and E_h are electron and hole energies, and V is the total volume of the system.

The oscillator strength f of the exciton [Eqs. (40), (41)] can be calculated as

$$f = \frac{2\hbar^2}{m_0 E_{\text{exc}}} \sum_\alpha \left| \int_V d\mathbf{r} \psi_e^*(\mathbf{r})(\mathbf{e}, \hat{\mathbf{k}}) \psi_h^{(\alpha)}(\mathbf{r}) \right|^2, \tag{42}$$

where $\mathbf{e}$ is the polarization of incident light, $\hat{\mathbf{k}} = -i\nabla$ is the wave vector operator, and α denotes different hole wave functions corresponding to the same degenerate hole energy level E_h. To calculate the oscillator strength f, the integral over the volume V in Eq. (42) should be represented as a sum of integrals over unit cells contained in the volume V. When integrating over the volume of each unit cell, envelope wave functions Ψ_e and Ψ_h are treated as specific for each unit cell constants. In this case, each integral over the volume of a unit cell is proportional to the constant:

$$\langle S|\hat{k}_i|I\rangle = \delta_{i,I} \sqrt{\frac{m_0 E_P}{2\hbar^2}}, \tag{43}$$

which is equal for each unit cell of the same material. In Eq. (43) $i, I = X, Y, Z$; $\delta_{i,I}$ is the Kronecker delta symbol; and E_P is the Kane energy.

The oscillator strength f not only defines the strength of absorption lines, but also relates to the radiative decay time τ [17]:

$$\tau = \frac{2\pi\varepsilon_0 m_0 c^3 \hbar^2}{n e^2 E_{\text{exc}}^2 f}, \tag{44}$$

where ε_0, m_0, c, $\hbar$, and e are fundamental physical constants with their usual meaning and n is the refractive index.

2.2.3. Results of Calculation and Discussion

In the following we consider excitonic properties of WZ GaN/AlN, ZB GaN/AlN, and WZ $GaN/Al_{0.15}Ga_{0.85}N$ QDs as a function of QD height. The exciton energy has been calculated using Eq. (41), where the Coulomb potential energy (36) has been computed with the help of a finite-difference method. Figure 10(a) shows exciton ground state energy levels as a function of QD height for the three kinds of GaN QDs. Filled triangles, filled circles, and

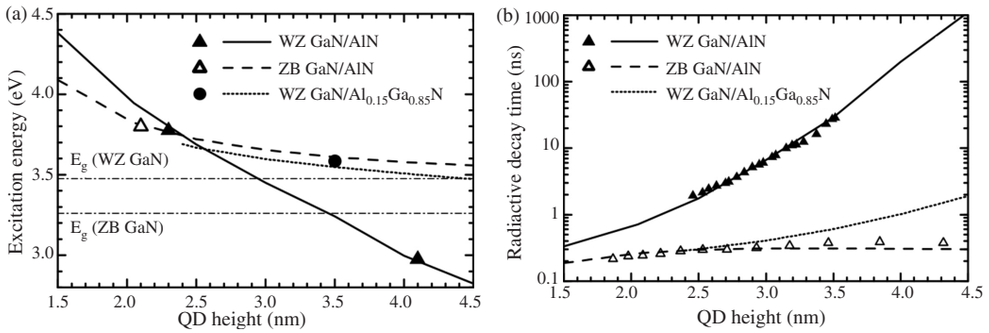

Figure 10. Exciton ground state energy levels (a) and radiative decay time (b) as a function of QD height for three kinds of GaN QDs. In (a), filled triangles represent experimental points of Widmann et al. [2]; empty triangle is an experimental point of Daudin et al. [8]; and filled circle is an experimental point of Ramval et al. [4]. Dash-dotted lines indicate bulk energy gaps of WZ GaN and ZB GaN. In (b), filled and empty triangles represent experimental points from Ref. [18] for WZ GaN/AlN and ZB GaN/AlN QDs, respectively. Exciton energy and radiative decay time in WZ GaN/$Al_{0.15}Ga_{0.85}N$ QDs are shown only for those QD heights that allow both electron and hole discrete energy levels.

empty triangles, show experimental points from Refs. [2, 4, 8], correspondingly. The figure shows fair agreement between calculated exciton ground state energies and experimental data. It is seen that for WZ GaN/AlN QDs higher than 3 nm, the exciton ground state energy drops below the bulk WZ GaN energy gap. Such a huge red-shift of the exciton ground state energy with respect to the bulk WZ GaN energy gap is attributed to the strong piezoelectric field in WZ GaN/AlN QDs. Due to the lower strength of the piezoelectric field in WZ GaN/$Al_{0.15}Ga_{0.85}N$ QDs, the exciton ground state energy in these QDs becomes equal to the bulk WZ GaN energy gap only for a QD with height 4.5 nm. The piezoelectric field in ZB GaN/AlN QDs cannot significantly modify conduction and valence band edges, therefore the behavior of the exciton ground state energy with increasing QD height is mainly determined by the deformation potential and confinement.

Figures 5 and 6 show that the electron and hole are spatially separated in WZ GaN/AlN QDs. This fact leads to very small oscillator strength (42) in those QDs. On the other hand, the charges are not separated in ZB GaN/AlN QDs, resulting in a large oscillator strength. An important physical quantity, the radiative decay time (44) is inversely proportional to the oscillator strength. Calculated radiative decay times of excitonic ground state transitions in the three kinds of GaN QDs are plotted in Fig. 10(b) as a function of QD height. The amplitude of the piezoelectric potential in WZ GaN/AlN and GaN/$Al_{0.15}Ga_{0.85}N$ QDs increases with increasing the QD height. Therefore, the electron–hole separation also increases, the oscillator strength decreases, and the radiative decay time increases. The figure shows that the radiative decay time of the red-shifted transitions in WZ GaN/AlN QDs ($H>3$ nm) is large and increases almost exponentially from 6.6 ns for QDs with height 3 nm to 1100 ns for QDs with height 4.5 nm. In WZ GaN/$Al_{0.15}Ga_{0.85}N$ QDs, the radiative decay time and its increase with QD height are much smaller than those in WZ GaN/AlN QDs. The radiative decay time in ZB GaN/AlN QDs is found to be of order 0.3 ns and almost independent of QD height. Filled and empty triangles in Fig. 10(b) represent experimental points of Ref. [18], which appear to be in good agreement with our calculations.

Figures 11(a) and 11(b) show the results of the calculation of exciton energy levels and oscillator strengths corresponding to the first four optically active exciton states in WZ GaN/AlN QDs. The two states shown by solid (dashed) lines are active when the incoming light is polarized along the x-axis (y-axis). The exciton energy and oscillator strength in WZ GaN/AlN QDs depend on the in-plane polarization of the incoming light, because of the lack of the QD symmetry with the interchange of x and y coordinates. If the incoming light is randomly polarized in the x–y plane, each of the first two peaks in the absorption spectrum splits into a pair of two very close peaks. The distance between the two sets of peaks decreases from about 60 meV to about 40 meV with increasing the QD height from 1.5 nm to 4.5 nm. Such relatively small decrease of the energy difference can be explained by the

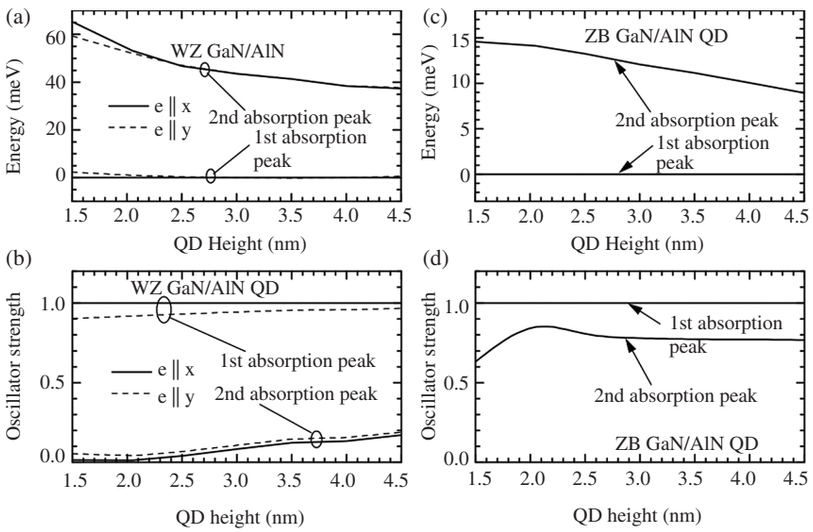

Figure 11. Energy and oscillator strength of first peaks in the absorption spectrum of WZ (a, b) and ZB (c, d) GaN/AlN QDs. Solid (dashed) lines correspond to the polarization of incoming light along the x-axis (y-axis). The energy in panels (a, c) and the oscillator strength in panels (b, d) are normalized to the first absorption peak when the light is polarized along the x-axis.

above mentioned fact that the effective volume occupied by electrons and holes increases only slightly with increasing the QD size. Figure 11(b) shows that the amplitude of the second set of absorption peaks is about 10 times smaller than it is for the first set of absorption peaks and it slightly increases with increasing the QD size.

Figures 11(c) and 11(d) show the calculated exciton energy levels and oscillator strengths corresponding to the first two optically active exciton states in ZB GaN/AlN QDs. Each of the two states shown in Fig. 5 is two-fold degenerate due to the QD symmetry with the interchange of x and y coordinates. The distance between the first two peaks in the absorption spectrum decreases from about 15 meV to about 10 meV with increasing the QD height from 1.5 nm to 4.5 nm. Similarly to WZ GaN/AlN QDs, such relatively small decrease of the energy difference can be explained by the fact that the effective volume occupied by electrons and holes increases only slightly with increasing the QD size. However, because the lateral size of ZB QDs is about two times the lateral size of WZ QDs, the energy difference between the first two absorption peaks in ZB QDs is about 4 times smaller than it is in the WZ QDs. Figure 11(d) shows that unlike WZ GaN/AlN QDs, the amplitude of the second absorption peak in ZB GaN/AlN QDs is comparable with the amplitude of the first absorption peak and it changes non-monotonically with increasing QD size.

3. ZnO QUANTUM DOTS

ZnO has recently attracted significant attention as a promising material for applications in UV light-emitting diodes, laser diodes, varistors, and transparent conducting films. Compared to other wide band-gap materials, ZnO has a very large exciton binding energy ($\sim$60 meV), which results in more efficient excitonic emission at room temperature. It is well known that semiconductor nanocrystals or QDs may have superior optical properties than bulk crystals owing to quantum confinement effects [19]. For example, it has been experimentally established that the third-order nonlinear susceptibility of ZnO nanocrystals is $\sim$500 larger that that of bulk ZnO [20]. A well-established fabrication technique, which utilizes colloidal suspension [20–26], gives ZnO QDs of nearly spherical shape with diameters less than 10 nm. Thus, optical properties of colloidal ZnO QDs, such as exciton energy and radiative lifetime, are expected to be strongly affected by quantum confinement.

3.1. Excitonic Properties of Wurtzite ZnO Quantum Dots

Interpretation of experimental data and optimization of ZnO QDs for optoelectronic device applications require a theoretical model for prediction of the energy and the oscillator strength of optical transitions. Due to specifics of WZ ZnO material system, such as degeneracy and anisotropy of the valence band as well as small dielectric constant and correspondingly strong electron—hole Coulomb interaction, simple one-band effective-mass models fail to give correct results. Recently, the tight-binding method has been used to compute the electron and hole states in ZnO QDs [27]. The electron–hole interaction in Ref. [27] has been taken into account by adding the exciton binding energy of $-1.8e^2/\varepsilon R$ [28] to the energy of an electron–hole pair. However, Brus [29] has shown that the treatment of an exciton in ZnO QDs as an electron–hole pair is a rather poor approximation leading to significant errors. The pseudopotential model, which was shown to describe exciton states in a CdSe QD [30] very well, to the best of our knowledge, has not been applied to ZnO QDs.

In this chapter we focus on the properties of the lowest excitonic states in colloidal nearly spherical ZnO QDs with diameters in the range from 2 nm to 6 nm. Fonoberov et al. [31] have demonstrated that the multiband effective-mass model works surprisingly well for the description of lowest exciton states even for the quantum shells [32] as thin as one monolayer. Here, we employ this model, with some modifications [33], to calculate the lowest exciton states in ZnO QDs. In our numerical computations we use the effective-mass parameters listed in Ref. [34]. Since the exciton Bohr radius a_B in bulk ZnO is about 0.9 nm [34], the size of the considered QDs is two-three times larger than the size of the bulk exciton. The latter results in a situation when the strength of the electron–hole Coulomb interaction and quantum confinement effects are comparable. Therefore, one cannot use either the "strong confinement" or "weak confinement" approximations [35] to obtain exciton states in such ZnO QDs. The strong confinement approximation ($R/a_B <\sim 2$) assumes that the electron and hole confinement energies are much larger than the Coulomb interaction energy and the electron and hole wave functions can be treated separately. The weak confinement limit ($R/a_B >\sim 4$) uses the assumption that Coulomb interaction is strong compared to quantum confinement and, as a result, the exciton wave function can be decomposed into the wave function of the exciton center of mass and the wave function of the relative electron–hole motion.

To determine excitonic states in ZnO QDs in the "intermediate confinement" regime, which is relevant to the reported experimental data and important for possible device applications, we solve the six-dimensional exciton problem. In the case of isotropic nondegenerate conduction and valence bands the aforementioned six-dimensional problem for spherical QDs can be reduced to a three-dimensional one with independent variables r_e, r_h, and θ', where θ' is the angle between the electron radius-vector $\mathbf{r}_e$ and hole radius-vector $\mathbf{r}_h$. However, the valence band of ZnO is degenerate and anisotropic. Therefore, we can only reduce the exciton problem to a five-dimensional one by making use of the axial symmetry of exciton wave functions along the c-axis of WZ ZnO. We calculate the exciton states using the following Hamiltonian

$$\hat{H}_{\text{exc}} = [\hat{H}_e + V_{s-a}(\mathbf{r}_e)] - [\hat{H}_h - V_{s-a}(\mathbf{r}_h)] + V_{\text{int}}(\mathbf{r}_e, \mathbf{r}_h), \tag{45}$$

where the two-band electron and the six-band hole Hamiltonians $\hat{H}_e$ and $\hat{H}_h$ for WZ nanocrystals have been written explicitly in Ref. [10]. Since dielectric constants in ZnO QD and the exterior medium are different the Coulomb potential energy of the electron–hole system in Eq. (45) is represented by the sum of the electron–hole interaction energy $V_{\text{int}}(\mathbf{r}_e, \mathbf{r}_h)$ and electron and hole self-interaction energies $V_{s-a}(\mathbf{r}_e)$ and $V_{s-a}(\mathbf{r}_h)$ defined in Refs. [16, 29]. Neglecting a very small spin-orbit splitting, which is about 10 meV [36, 37] for ZnO, we can simplify the exciton problem by using the one-band electron and the three-band hole Hamiltonians.

We choose the coordinate system in such a way that the z-axis is parallel to the c-axis of WZ ZnO. Due to the axial symmetry of the exciton problem, the z-component of the exciton angular momentum M_z is a good quantum number. To compute the eigenstates of

the Hamiltonian (45) we represent the three-component exciton envelope function in the form:

$$\Psi_{M_z}(\mathbf{r}_e, \mathbf{r}_h) = \frac{1}{2\pi} \sum_{m=-\infty}^{\infty} \begin{pmatrix} \Psi_{-1}^{M_z,m}(\rho_e, z_e; \rho_h, z_h) e^{i(m-1)\varphi} \times e^{i(M_z-1)\Phi} \\ \Psi_{0}^{M_z,m}(\rho_e, z_e; \rho_h, z_h) e^{im\varphi} \times e^{iM_z\Phi} \\ \Psi_{1}^{M_z,m}(\rho_e, z_e; \rho_h, z_h) e^{i(m+1)\varphi} \times e^{i(M_z+1)\Phi} \end{pmatrix}, \tag{46}$$

where Ψ_{-1}, Ψ_0, and Ψ_1 are the components of exciton envelope function in front of the Bloch functions $|(S(X+iY)/\sqrt{2}\rangle$, $|SZ\rangle$, and $|(S(X-iY))/\sqrt{2}\rangle$, respectively. In Eq. (46) the angles φ and Φ describe the relative angular motion of the electron and the hole and their angular motion as a whole, correspondingly. Substitution of the wave function (46) into the envelope-function equation with Hamiltonian (45) gives the system of three five-dimensional differential equations with respect to functions $\Psi_{\alpha}^{M_z,m}(\rho_e, z_e; \rho_h, z_h)$. The obtained system is solved numerically using the finite-difference method. In the numerical calculation we have neglected the small penetration of the exciton wave function into the exterior medium.

To validate the model we calculated exciton ground state energy as a function of the QD radius for spherical ZnO QDs in water and compared it with experimental data reported in Refs. [22, 23]. As one can see in Fig. 12, our theoretical results are in excellent agreement with measurements. We have studied the influence of the QD shape and the exterior medium on the exciton ground state energy. Transmission electron microscopy (TEM) images of ZnO QDs show that a fraction of QDs are not spherical but rather prolate ellipsoids with the ratio of semi-axes of about 9/8 [23]. Our calculations show that prolate ZnO QDs have smaller exciton ground state energy than spherical QDs with the same semi-minor axis (shown by the dashed line in Fig. 12). If we consider ZnO QDs in air ($\varepsilon = 1$) instead of water ($\varepsilon = 1.78$), the exciton ground state energy increases (shown by the dotted line in Fig. 12). The difference in the ground state energies due to the change of the ambient (water $\rightarrow$ air) decreases from 70 meV to 13 meV when the QD radius increases from 1 nm to 3 nm. Overall it is seen from our calculations that small size dispersion of ZnO QDs and different exterior media have relatively small influence on the exciton ground state energy for the QDs with radius above 1.5 nm.

Interpretation of experimental data as well as prediction of the optical properties for ZnO QDs requires the knowledge of transition energies and their oscillator strength. The size dependence of the excited exciton states in spherical ZnO QDs is shown in Fig. 13. The energy of the excited states is counted from the exciton ground state energy. Figure 13 shows the size dependence of few lowest exciton states with $|M_z| = 0, 1, 2$. The oscillator strength

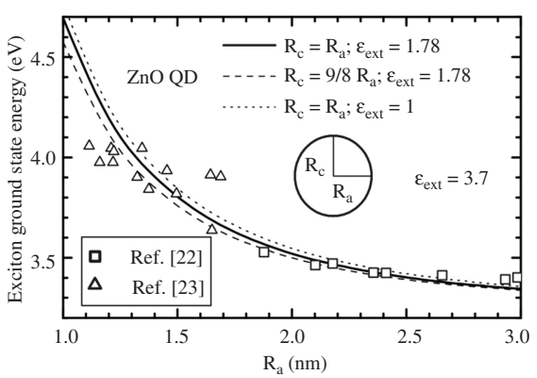

Figure 12. Calculated exciton ground state energy in ZnO QDs as a function of the QD radius (semi-axis) for spherical (ellipsoidal) QDs. Results are shown for two different ambient media: water ($\varepsilon = 1.78$) and air ($\varepsilon = 1$). For comparison we show experimental data points from Refs. [22, 23]. Reprinted with permission from [33], V. A. Fonoberov and A. A. Balandin, *Phys. Rev. B* 70, 195410 (2004). © 2004, American Physical Society.

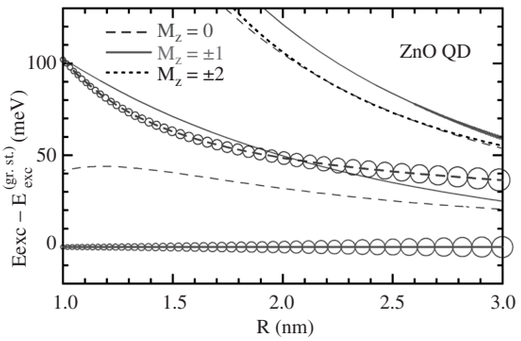

Figure 13. Energies of the excited exciton states (counted from the exciton ground state) as a function of the radius of spherical ZnO QD in water. The oscillator strength of the corresponding transitions is depicted with circles. The size of the circles is proportional to the oscillator strength. Reprinted with permission from [33], V. A. Fonoberov and A. A. Balandin, *Phys. Rev. B* 70, 195410 (2004). © 2004, American Physical Society.

f of an exciton state with energy E_{exc} and envelope wave function $\Psi_{\text{exc}}(\mathbf{r}_e, \mathbf{r}_h)$ is calculated as [10]

$$f = \frac{E_P}{E_{\text{exc}}} \left| \int_V \Psi_{\text{exc}}^{(\alpha)}(\mathbf{r}, \mathbf{r}) d\mathbf{r} \right|^2, \tag{47}$$

where the Kane energy of ZnO is $E_P = 28.2$ eV [38]. In Eq. (47) α denotes the component of the wave function, which is active for a given polarization. In the dipole approximation, only exciton energy levels with $|M_z| = 0, 1$ can be optically active, i.e., they can have a nonzero oscillator strength. Besides, the exciton energy levels with $M_z = 0$ ($M_z = \pm 1$) are optically active only for the polarization $\mathbf{e} \parallel \mathbf{z}$ ($\mathbf{e} \perp \mathbf{z}$). The oscillator strengths of the corresponding exciton energy levels are depicted in Fig. 13 with circles. The size of the circles is proportional to the oscillator strength. We can see that there are two exciton levels that have large oscillator strengths. They are the first level with $|M_z| = 1$, which is the exciton ground state, and the second level with $M_z = 0$. The energy difference between the two exciton levels decreases while their oscillator strengths, which are almost the same for both levels, increase with the increasing the QD size. Other exciton energy levels shown in Fig. 13 have zero or negligible oscillator strength.

Figure 14 shows the optically active component of the exciton wave function (with equal electron and hole coordinates) for each of the two brightest exciton states from Fig. 13

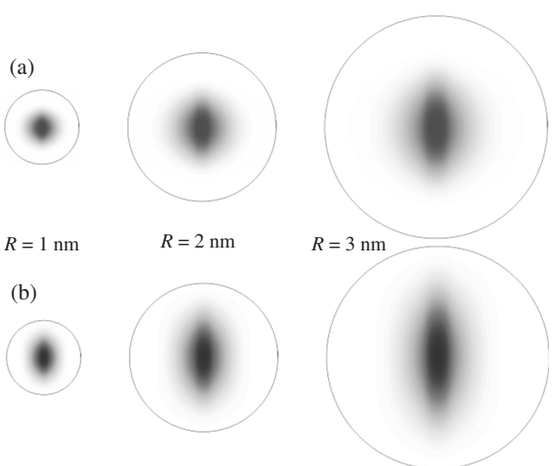

Figure 14. Optically active component of the exciton wave function (with equal electron and hole coordinates) of the first (a) and the second (b) bright exciton states for three different sizes of spherical ZnO QDs in water. The c-axis of WZ ZnO is directed vertically.

for QD radii 1 nm, 2 nm, and 3 nm. For QDs with $R > a_B$, the electron and hole motion around their center of mass prevents the center of mass from reaching the QD surface, thus, forming a so-called dead layer near the QD surface. The concept of the exciton dead layer can be traced back to Pekar [39]. It states that the exciton is totally reflected from an effective barrier located inside the QD at the distance d from the QD surface. To estimate the thickness d of the dead layer in ZnO QDs, we assume that only the optically active component of the exciton wave function is nonzero, what allows us to approximate the wave function of the exciton center of mass as

$$\Psi_{\text{exc}}(\mathbf{r}, \mathbf{r}) = \frac{1}{\sqrt{\pi a_B^3}} \frac{\sin(\pi r/(R-d))}{r\sqrt{2\pi(R-d)}}. \tag{48}$$

Assuming that Eq. (48) correctly reproduces the density of the exciton's center of mass, we can find the thickness d of the dead layer and the exciton Bohr radius a_B from the following system:

$$\begin{cases} \sqrt{\dfrac{8(R-d)^3}{\pi^2 a_B^3}} = \displaystyle\int_V \Psi_{\text{exc}}^{(\alpha)}(\mathbf{r}, \mathbf{r}) d\mathbf{r}, \\ \dfrac{1}{\sqrt{2a_B^3(R-d)^3}} = \Psi_{\text{exc}}^{(\alpha)}(0, 0). \end{cases} \tag{49}$$

Note that the system (49) is an identity when the optically active component $\Psi_{\text{exc}}^{(\alpha)}(\mathbf{r}, \mathbf{r})$ of the wave function of exciton ground state is given by Eq. (48). The fitting parameters d and a_B found as solutions of system (49) are plotted in Fig. 15 as a function of the radius of ZnO QD in water. The quality of the fit is illustrated in Fig. 16 for the ZnO/water QD with $R = 2$ nm. It is seen from Fig. 15 that the dead-layer thickness d increases almost linearly with R while the exciton Bohr radius tends to its bulk value (0.9 nm). Figure 14 confirms that the thickness of the dead layer increases with increasing the QD size. Our estimate gives the value of the dead-layer thickness $d = 1.6$ nm for $R = 3$ nm, what almost coincides with the dead-layer thickness calculated in Ref. [40] for a quantum well with thickness $L \gg a_B$ and $m_{hh}/m_e = 9.5$ [34]. The latter suggests that the thickness of the dead layer for larger ZnO QDs, i.e., in the weak confinement regime, is not noticeably larger than 1.6 nm. The relatively large thickness of the dead layer in colloidal ZnO QDs is attributed to the large ratio of hole and electron effective masses.

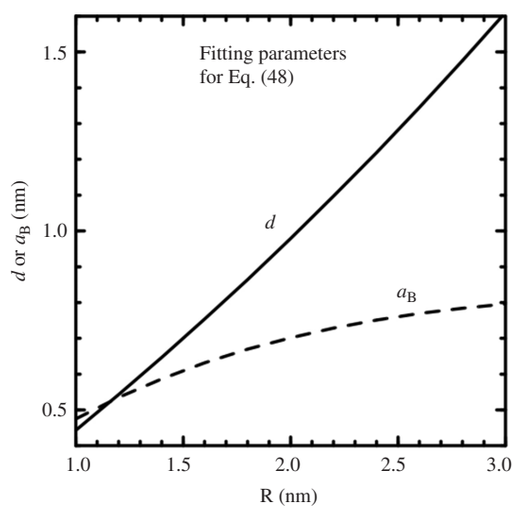

Figure 15. Fitting parameters for Eq. (48) as a function of ZnO QD radius; d is the dead layer thickness and a_B is the exciton Bohr radius.

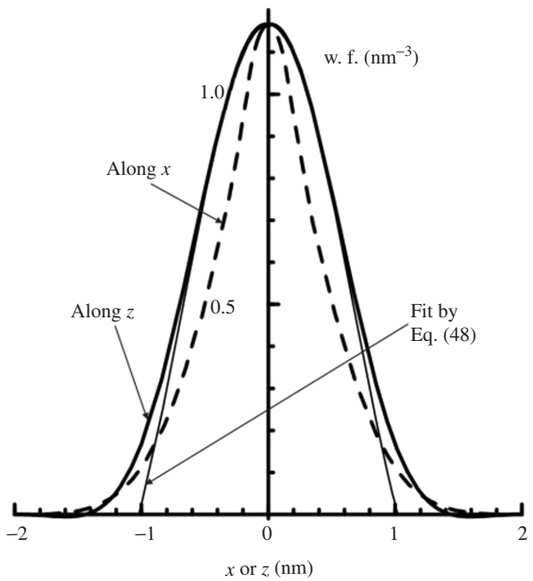

Figure 16. Wave function of the exciton's center of mass along x and z axes for the 4 nm in diameter ZnO QD; thin solid line shows a fit by Eq. (48).

The fact that the exciton in the spherical ZnO QDs is prolate along the c-axis (see Fig. 14) is attributed to the anisotropy of valence band of WZ ZnO. It is also seen from Fig. 14 that the exciton is more prolate for the second optically active state than it is for the first one. Figure 17 compares the distribution of an electron over the volume of the 4 nm in diameter ZnO QD with the distribution of the exciton's center of mass over the same volume. Keeping in mind that the conduction band of WZ ZnO is isotropic and the electron can occupy the entire volume of the QD (no dead layer), the characteristic features of the exciton in the ZnO QD are clearly seen. The exciton center of mass is prolate along the c-axis of WZ ZnO and squeezed to the center of the ZnO QD. The above behavior of the exciton in a colloidal ZnO QD should strongly affect the exciton radiative lifetime.

The radiative recombination lifetime τ of excitons in bulk ZnO is about 322 ps [41], which is small compared to other semiconductors. It is well known that the oscillator strength of localized excitons is substantially higher than that of free excitons [42]. Since the excitons are confined in ZnO QDs and the radiative lifetime is inversely proportional to the oscillator strength [see Eq. (44)], one can expect for ZnO QDs very small exciton radiative lifetimes of the order of tens of picoseconds. To the best of our knowledge, no measurements of the exciton lifetime in ZnO QDs have been carried out. However, it has been established that the exciton lifetime is less than 50 ps for QDs with diameter 5 nm [21].

The calculated radiative lifetime of the excitons in the ground state are shown in Fig. 18 as the function of the QD size. The solid line in Fig. 18 represents the radiative lifetime in

Figure 17. Distribution of the probability density of an electron and an exciton (center of mass) over the volume of the 4 nm in diameter spherical ZnO QD. The innermost and middle isosurfaces contain 1/3 and 2/3 of the total probability density, respectively.

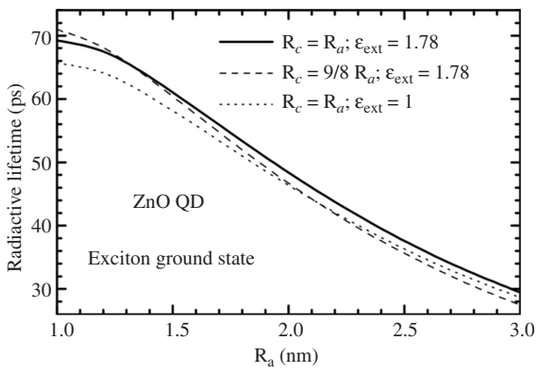

Figure 18. Radiative lifetime of the exciton ground state in ZnO QDs as a function of the QD radius (semi-axis) for spherical (ellipsoidal) QDs. Reprinted with permission from [33], V. A. Fonoberov and A. A. Balandin, *Phys. Rev. B* 70, 195410 (2004). © 2004, American Physical Society.

the spherical ZnO QD in water, the dashed line shows the lifetime in the prolate ZnO QD in water, and the dotted line gives the lifetime in the spherical ZnO QD in air. For the QD with diameter 5 nm we get the lifetime of about 38 ps, in agreement with the conclusion of Ref. [21]. We can see that the influence of the QD ellipticity and the exterior medium on the radiative lifetime in ZnO QDs is relatively weak. Analyzing the calculated dependence of the exciton lifetime on the radius of the spherical ZnO QD in water, we found that it can be fitted accurately with the function $\tau_o/[1 + (R/R_o)^3]$, where $\tau_o = 73.4$ ps and $R_o = 2.55$ nm. For larger QDs, i.e., in the weak confinement regime, the exciton lifetime is known to be inversely proportional to the QD volume. Indeed, in this case substituting Eq. (48) into Eq. (47) one estimates $f \sim (R - d)^3/a_B^3$ and, therefore,

$$\tau \sim a_B^3/(R - d)^3.$$

3.2. Effect of Surface Impurities on the Optical Response of ZnO Quantum Dots

Lately, there have been a number of reports of fabrication, structural and optical characterization of ZnO QDs [20–26, 44]. Different fabrication techniques [24, 44] and methods of the QD surface modification [20, 25] have been used to quench the defect-related green PL and enhance the UV emission from ZnO QDs. However, the nature of the UV PL from ZnO QDs itself is not fully understood. Some authors attribute the UV PL to the recombination of confined excitons [21], while others argue that the emission comes from surface impurities or defects [20].

Understanding the origin of UV PL in ZnO QDs is important from both fundamental science and proposed optoelectronic applications points of view. In this chapter we address this issue by examining theoretically the optical properties of ZnO QDs with and without ionized impurities at the QD surface. We limit our consideration to spherical QDs with diameters in the range from 2 nm to 6 nm, because common fabrication techniques [20–26, 44] give nearly spherical ZnO QDs with diameter less than 10 nm.

There are only few reports on the calculation of exciton states in the presence of charges at the QD surface [45–47]. Using the empirical pseudopotential method Wang et al. [45, 46] studied the influence of an external charge on the electron–hole pair in the spherical CdSe QD. The electron–hole interaction in Ref. [46] was averaged so that the exciton problem was reduced to two single particle problems. While this is a good approximation for the 4 nm diameter CdSe QDs, it is not acceptable for ZnO QDs of the same size. This difference comes from the fact that the exciton Bohr radius in ZnO is only 0.9 nm [34]. Since the size of ZnO QDs is only two-three times larger than the size of the exciton, the electron–hole interaction and quantum confinement effects have comparable strengths. Therefore, a two particle problem has to be solved for an exciton in ZnO QDs.

The solution of a two particle problem is a challenging task for atomistic tight-binding or pseudopotential methods. On the other hand, the multiband effective-mass method works surprisingly well for the description of lowest exciton states even for quantum shells as thin as one monolayer [31]. To solve the six-dimensional exciton problem (it can be reduced to a five-dimensional one by making use of the axial symmetry of exciton wave functions along the *c*-axis in WZ ZnO) we employ the latter method adapted by us for ZnO QDs in Ref. [47].

The exciton Hamiltonian with and without an ionized impurity present at the QD surface is written as

$$\hat{H}_{\text{exc}} = [\hat{H}_e + V_{s-a}(\mathbf{r}_e)] - [\hat{H}_h - V_{s-a}(\mathbf{r}_h)] + V_{\text{int}}(\mathbf{r}_e, \mathbf{r}_h) + \alpha(V_{\text{int}}(\mathbf{R}, \mathbf{r}_e) - V_{\text{int}}(\mathbf{R}, \mathbf{r}_h)), \quad (50)$$

where the two-band electron and the six-band hole Hamiltonians $\hat{H}_e$ and $\hat{H}_h$ for WZ nanocrystals have been introduced by us earlier in this chapter. Since the dielectric constants of ZnO QD and of the exterior medium are different, the Coulomb potential energy of the electron–hole system in Eq. (50) is represented by the sum of the electron–hole interaction energy $V_{\text{int}}(\mathbf{r}_e, \mathbf{r}_h)$ and electron and hole self-interaction energies $V_{s-a}(\mathbf{r}_e)$ and $V_{s-a}(\mathbf{r}_h)$, which are calculated numerically after Ref. [16]. In the last term of Eq. (50), $\mathbf{R}$ is the radius-vector of the impurity and α is the charge of the impurity in units of $|e|$ ($\alpha = 1$ for a donor, $\alpha = -1$ for an acceptor, and $\alpha = 0$ when there is no impurity). The z-axis is chosen to be parallel to the c-axis of WZ ZnO. Therefore, we consider an impurity located on the z-axis to keep the axial symmetry of the problem. To calculate the exciton states we neglect the small penetration of the exciton wave function into the exterior medium and solve the Schrödinger equation with Hamiltonian (50) using the finite-difference method [16] (a cubic grid with unit length of 0.05 nm has been used, what ensured the relative error for the exciton ground state energy <1%). The material parameters employed for ZnO are listed in Ref. [34].

The results of our calculation for an exciton confined in spherical ZnO QD in water are shown in Fig. 19. It is seen from Fig. 19(a) that the wave function of the exciton ground state with equal electron and hole coordinates, i.e., the exciton center of mass, is prolate along the *c*-axis of WZ ZnO. It is also seen that the thickness of the dead layer [33] increases with QD size. Note that the above features, which have a strong influence on the optical properties, can be obtained only if the electron–hole interaction is taken into account exactly.

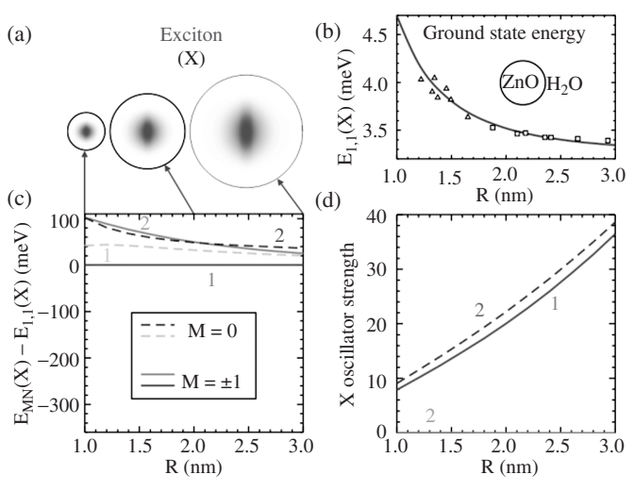

Figure 19. (a) Wave functions of exciton center of mass for three ZnO QDs with different sizes. (b) Calculated exciton ground state energy as a function of the QD radius (ambient medium is water) and experimental points from Ref. [22] (boxes) and Ref. [23] (triangles). (c) Lowest exciton energy levels counted from the ground state energy. (d) Exciton oscillator strength as a function of the QD radius. Solid (dashed) lines correspond to $|M| = 1$ ($M = 0$). Reprinted with permission from [47], V. A. Fonoberov and A. A. Balandin, Appl. Phys. Lett. 85, 5971 (2004). © 2004, American Institute of Physics.

Figure 19(b) shows calculated ground state energy of confined excitons as a function of the QD radius. As one can see, our theoretical results are in excellent agreement with experimental data reported in Refs. [22, 23]. If we consider ZnO QDs in air ($\varepsilon = 1$) instead of water ($\varepsilon = 1.78$), the exciton ground state energy slightly increases. The energy difference due to the change of the ambient (water $\rightarrow$ air) decreases from 70 meV to 13 meV when the QD radius increases from 1 nm to 3 nm.

Due to the axial symmetry of the exciton problem, the z-component M of the exciton angular momentum is a good quantum number. The size dependence of the four lowest exciton energy levels with $|M| = 0, 1$ is shown in Fig. 19(c) relative to the ground state energy, which has $M = \pm 1$. In an absorption spectrum, the intensity of an exciton state with energy E_{exc} and envelope wave function $\Psi_{\text{exc}}(\mathbf{r}_e, \mathbf{r}_h)$ is characterized by the oscillator strength (47). In the dipole approximation, only exciton energy levels with $|M| = 0, 1$ can be optically active, i.e., they can have a nonzero oscillator strength. Besides, the exciton energy levels with $M = 0$ ($M = \pm 1$) are optically active only for the polarization $\mathbf{e} \parallel \mathbf{z}$ ($\mathbf{e} \perp \mathbf{z}$). Figure 19(d) shows the oscillator strengths of the exciton energy levels presented in Fig. 19(c). Note that the oscillator strength of the first energy level with $M = 0$ is not shown; because it is found to be zero for all considered QD sizes.

Analogously to Fig. 19, calculated optical properties of ionized donor–exciton, and ionized acceptor–exciton complexes in spherical ZnO QDs are presented in Fig. 20. It is seen from Fig. 20(a) that the dead layer is observed near the QD surface for the ionized donor–exciton complex. On the contrary, Fig. 20(b) shows that the ionized acceptor–exciton complex is located in the vicinity of the acceptor. This means that the exciton is bound to the surface-located acceptor. Unlike the acceptor, the donor does not bind the exciton. Figures 20(c) and 20(d) show the size dependence of the four lowest exciton energy levels with $|M| = 0, 1$

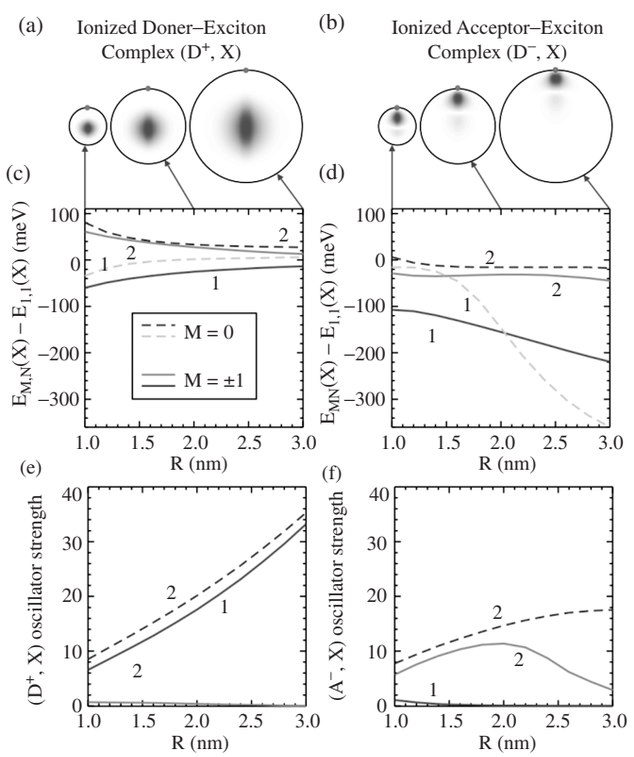

Figure 20. (a)–(b) Wave functions of exciton center of mass for three ZnO QDs with different sizes. (c)–(d) Lowest energy levels of ionized impurity-exciton complexes counted from the exciton ground state energy [see Fig. 19(b)]. (e)–(f) Corresponding oscillator strengths as a function of the QD radius. Panels (a), (c), (e) and (b), (d), (f) show the calculated results in the presence of an ionized donor and ionized acceptor, respectively. Large dots show the position of the impurity. Solid (dashed) lines correspond to $|M| = 1$ ($M = 0$). Reprinted with permission from [47], V. A. Fonoberov and A. A. Balandin, Appl. Phys. Lett. 85, 5971 (2004). © 2004, American Institute of Physics.

in the ZnO QDs with surface impurities. The energy levels are counted from the ground state energy of the confined exciton (no impurities). It is seen that the absolute value of the plotted energy difference for the donor-exciton complex is small and decreases with QD size, while this absolute value is much larger and increases with QD size for the acceptor-exciton complex. Such a different behavior of the exciton energy levels is due to the fact that the hole is much heavier than the electron, what makes the surface donor a shallow impurity, while the surface acceptor a deep impurity. Therefore, excitons can be effectively bound only to surface acceptors.

Figures 20(e) and 20(f) show the oscillator strengths of the exciton energy levels from Figs. 20(c) and 20(d). We can see that for the confined excitons and ionized donor–exciton complexes there are two energy levels that have large oscillator strengths (the first level with $|M| = 1$ and the second level with $M = 0$). The energy difference between the two energy levels decreases while their oscillator strengths, which are almost the same for both levels, increase with increasing the QD size. On the other hand, the oscillator strength of the ground state of the ionized acceptor–exciton complex is very small and decreases with QD size. Instead, the second energy level, with $|M| = 1$, has large oscillator strength with a maximum for a QD with the radius of about 2 nm.

Summarizing the above observations, one can conclude that the absorption edge, which is defined by the first energy level with $|M| = 1$ for the confined exciton and for the ionized donor–exciton complex and by the second energy level with $|M| = 1$ for the ionized acceptor–exciton complex, depends on the presence of impurities relatively weekly and it is only few tens of meV lower in energy for the impurity-exciton complexes than it is for the confined excitons. On the contrary, the position of the UV PL peak, which is defined by the first energy level with $|M| = 1$ for all considered cases, is 100–200 meV lower in energy for the ionized acceptor–exciton complex than it is for the confined exciton or the ionized donor–exciton complex. Most of the fabrication techniques, e.g., wet chemical synthesis [21, 23], produce ZnO QDs, which have the position of the UV PL peak close to the absorption edge. We can attribute the UV PL in such QDs to confined excitons. The surface of such QDs may contain donors, which only slightly affect the UV PL. Other fabrication techniques, such as the wet chemical synthesis in the presence of a polymer [20], produce ZnO QDs, which have the UV PL peak redshifted from the absorption edge as far as few hundreds of meV. We argue that this redshift may be caused by the presence of acceptors at the surface of ZnO QDs. The ionized acceptors, e.g., $(NaO)^-$, are more likely to be at the QD surface than inside the QD, because the latter fabrication techniques include some type of surface passivation. For example, the method described in Ref. [20] produces ZnO QDs capped with the polyvinyl pyrrolidone (PVP) polymer.

In the following, we suggest that the presence of acceptors at the surface of ZnO QDs can be determined by measuring the exciton radiative lifetime. As we mentioned earlier, the radiative recombination lifetime τ of excitons in bulk ZnO is about 322 ps. It has been established that the lifetime of confined excitons is less than 50 ps for QDs with diameter 5 nm [21]. Figure 21 shows the radiative lifetime as the function of the QD radius for the confined excitons as well as for the impurity–exciton complexes. It is seen that the radiative lifetime of the confined exciton and that of the ionized donor–exciton complex are almost the same; they decrease with QD size and are about an order of magnitude less (for $R \sim 2$ nm) than the bulk exciton lifetime. For the QD with diameter 5 nm we get the lifetime of 38 ps, in agreement with the conclusion of Ref. [21]. On the other hand, the radiative lifetime of the ionized acceptor–exciton complex increase with QD size very fast and it is about two orders of magnitude larger (for $R \sim 2$ nm) than bulk exciton lifetime.

In summary, depending on the fabrication technique and ZnO QD surface quality, the origin of UV PL in ZnO QDs is either recombination of confined excitons or surface-bound ionized acceptor–exciton complexes. In the latter case the Stokes shift of the order of 100–200 meV should be observed in the PL spectrum. The exciton radiative lifetime can be used as a probe of the exciton localization.

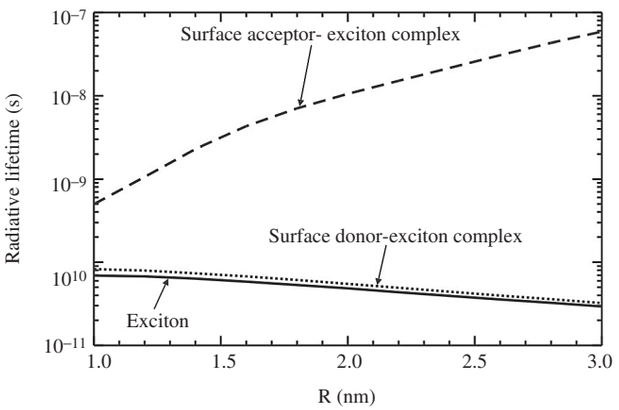

Figure 21. Radiative lifetime of confined excitons (solid line) and ionized impurity–exciton complexes (dotted and dashed lines) for ZnO QDs as a function of the QD radius.

3.3. Interface and Confined Polar Optical Phonons in ZnO Quantum Dots

It is well known that in QDs with ZB crystal structure there exist confined phonon modes with the frequencies equal to those of bulk transverse optical (TO) and longitudinal optical (LO) phonons and interface phonon modes with the frequencies intermediate between those of TO and LO modes [48]. Interface and confined optical phonon modes have been found for a variety of ZB QDs such as spherical [48], spheroidal [49, 50], multilayer spherical [51], and even multilayer tetrahedral [31] QDs. The calculated frequencies of optical phonon modes have been observed in the Raman, absorption, and PL spectra of ZB QDs [31, 52]. Lately, QDs with WZ crystal structure, such as ZnO and GaN nanostructures, have attracted attention as very promising candidates for optoelectronic, electronic, and biological applications. At the same time, only few reports have addressed the problem of polar optical phonons in WZ nanostructures [53, 54]. The solution obtained in Ref. [53] is approximate, i.e., uses *a priori* selected exponential dependence for the phonon potential, and provides an estimate only for interface optical phonon modes.

The frequencies of optical phonons in small covalent nanocrystals depend on the nanocrystal size, because the nanocrystal boundary causes an uncertainty in the phonon wave vector, which results in the redshift and broadening of the phonon peak. While the above size-dependence is important for very small covalent nanocrystals, it is negligible in the ionic ZnO QDs with sizes larger than 4 nm. The latter is due to the fact that the polar optical phonons in ZnO are almost non-dispersive in the region of small wave vectors. Since most of the reported experimental data is for ZnO QDs with sizes larger than 4 nm, in the following we assume that the polar optical phonons are non-dispersive in the relevant range of the wave vectors. Due to the uniaxial anisotropy of WZ QDs, the confined and interface optical phonon modes in such QDs should be substantially different from those in ZB (isotropic) QDs [54]. The main difference comes from the anisotropy of the dielectric function of WZ crystals. In order to describe the dielectric function, we employ the Loudon model, which is widely accepted for the WZ nanostructures [55, 56]. For example, the components of the dielectric tensor of WZ ZnO are [57]:

$$\varepsilon_{\perp}(\omega) = \varepsilon_{\perp}(\infty)\frac{\omega^2 - (\omega_{\perp,\mathrm{LO}})^2}{\omega^2 - (\omega_{\perp,\mathrm{TO}})^2}; \quad \varepsilon_z(\omega) = \varepsilon_z(\infty)\frac{\omega^2 - (\omega_{z,\mathrm{LO}})^2}{\omega^2 - (\omega_{z,\mathrm{TO}})^2}, \tag{51}$$

where the optical dielectric constants $\varepsilon_{\perp}(\infty)$ and $\varepsilon_z(\infty)$; LO phonon frequencies $\omega_{\perp,\mathrm{LO}}$ and $\omega_{z,\mathrm{LO}}$; and TO phonon frequencies $\omega_{\perp,\mathrm{TO}}$ and $\omega_{z,\mathrm{TO}}$ of bulk WZ ZnO are taken form Ref. [58]. The components of the dielectric tensor of some ternary WZ crystals such as $Mg_xZn_{1-x}O$ ($x < 0.33$) have more complex frequency dependence [59]:

$$\varepsilon_{\perp}(\omega) = \varepsilon_{\perp}(\infty)\frac{\omega^2 - (\omega_{\perp 1,\mathrm{LO}})^2}{\omega^2 - (\omega_{\perp 1,\mathrm{TO}})^2}\frac{\omega^2 - (\omega_{\perp 2,\mathrm{LO}})^2}{\omega^2 - (\omega_{\perp 2,\mathrm{TO}})^2}; \quad \varepsilon_z(\omega) = \varepsilon_z(\infty)\frac{\omega^2 - (\omega_{z,\mathrm{LO}})^2}{\omega^2 - (\omega_{z,\mathrm{TO}})^2}. \tag{52}$$

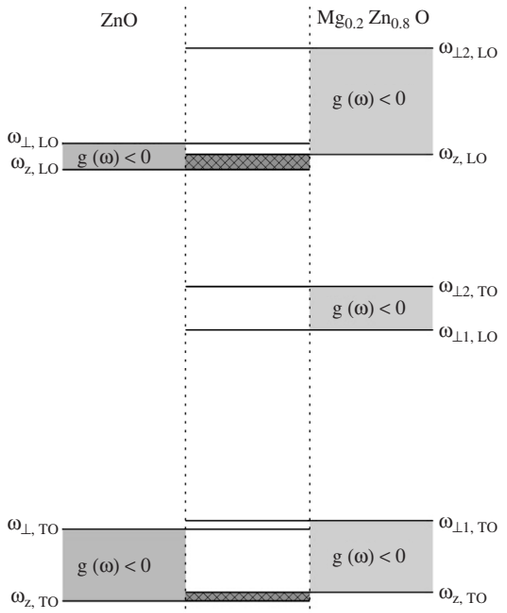

Figure 22. Zone center optical phonon frequencies of ZnO and $Mg_{0.2}Zn_{0.8}O$. Shaded regions correspond to the condition $g(\omega) < 0$ [see Eq. (65)]. Cross-hatched regions correspond to the condition $g(\omega) < 0$ for ZnO and $g(\omega) > 0$ for $Mg_{0.2}Zn_{0.8}O$.

The corresponding material parameters from Eq. (52) for bulk WZ $Mg_{0.2}Zn_{0.8}O$ are also taken from Ref. [58]. Zone center optical phonon frequencies of WZ ZnO and $Mg_{0.2}Zn_{0.8}O$ are shown in Fig. 22. Since there are only two zone center optical phonon frequencies (one LO and one TO) in ZB crystals, the phonon band structure of WZ crystals is more complex than that of ZB crystals. It will be shown in the following that the latter fact leads to polar optical phonon modes in WZ QDs that are strongly different from those in ZB QDs.

The description of the interface and confined polar optical phonons in this Section mostly follows our derivation given in Refs. [54, 58]. First, we present the analytical derivation of the polar optical phonon modes in spheroidal QDs with WZ crystal structure. Then, we apply our theory to a freestanding spheroidal ZnO QD and to a spheroidal ZnO QD embedded into a $Mg_{0.2}Zn_{0.8}O$ crystal.

3.3.1. Theory of Polar Optical Phonons in Wurtzite Quantum Dots

Let us consider a spheroidal QD with WZ crystal structure and with semi-axes a and c. The coordinate system (x, y, z') is chosen in such a way that the semi-axis c is directed along the symmetry axis z' of the QD. The equation of the QD surface is

$$\frac{x^2 + y^2}{a^2} + \frac{z'^2}{c^2} = 1. \tag{53}$$

After we introduce a new coordinate z such as

$$z' = \frac{c}{a} z \tag{54}$$

and transform the new Cartesian coordinates (x, y, z) into spherical coordinates (r, θ, ϕ), the Eq. (53) of the QD surface becomes $r = a$. In the following description we assume that the QD (medium $k = 1$) is embedded in a WZ crystal (medium $k = 2$). A freestanding QD can be easily considered as a special case.

Within the framework of the dielectric-continuum approximation, the potential $V(\mathbf{r})$ of polar optical phonons satisfies the Maxwell's equation, which can be written in the coordinates $\mathbf{r} = (x, y, z)$ as

$$-\nabla(\hat{\varepsilon}(\omega, \mathbf{r})\nabla V(\mathbf{r})) = 0 \tag{55}$$

with the dielectric tensor $\hat{\varepsilon}(\omega, \mathbf{r})$ defined as

$$\hat{\varepsilon}(\omega, \mathbf{r}) = \begin{pmatrix} \varepsilon_{\perp}(\omega, \mathbf{r}) & 0 & 0 \\ 0 & \varepsilon_{\perp}(\omega, \mathbf{r}) & 0 \\ 0 & 0 & \frac{a^2}{c^2}\varepsilon_z(\omega, \mathbf{r}) \end{pmatrix}. \tag{56}$$

Note that the term a^2/c^2 appears in Eq. (56) due to the coordinate transformation (54). The dielectric tensor (56) is constant in both media:

$$\hat{\varepsilon}(\omega, \mathbf{r}) = \begin{cases} \hat{\varepsilon}_1(\omega), & r \le a \\ \hat{\varepsilon}_2(\omega), & r > a, \end{cases} \tag{57}$$

therefore it is convenient to split Eq. (55) into separate equations for each medium:

$$-\nabla(\hat{\varepsilon}_k(\omega)\nabla V_k(\mathbf{r})) = 0; \quad k = 1, 2 \tag{58}$$

and apply the corresponding boundary conditions:

$$V_1(a, \theta, \phi) = V_2(a, \theta, \phi); \tag{59}$$

$$D_1(a, \theta, \phi) = D_2(a, \theta, \phi), \tag{60}$$

where the projections of the displacement vector **D** on the outer normal **n** at the QD surface can be written as

$$D_k(a, \theta, \phi) = (\mathbf{n}(\mathbf{r})\hat{\varepsilon}_k(\omega)\nabla V_k(\mathbf{r}))|_{r=a}, \quad k = 1, 2. \tag{61}$$

The phonon potential $V_1(\mathbf{r})$ that satisfies Eq. (58) and is finite everywhere inside the QD can be found analytically in spheroidal coordinates (ξ_1, η_1, ϕ):

$$V_1(\mathbf{r}) = \frac{P_l^m(\xi_1)}{P_l^m(\xi_1^{(0)})} P_l^m(\eta_1) e^{im\phi}. \tag{62}$$

Analogously, the phonon potential $V_2(\mathbf{r})$ that satisfies Eq. (58) and vanishes far away from the QD can be found analytically in spheroidal coordinates (ξ_2, η_2, ϕ):

$$V_2(\mathbf{r}) = \frac{Q_l^m(\xi_2)}{Q_l^m(\xi_2^{(0)})} P_l^m(\eta_2) e^{im\phi}. \tag{63}$$

In Eqs. (62) and (63), P_l^m and Q_l^m are associated Legendre functions of the first and second kinds, respectively; the integers l ($l \ge 0$) and m ($|m| \le l$) are quantum numbers of the phonon mode. The spheroidal coordinates (ξ_k, η_k) are related to the spherical coordinates (r, θ) as

$$\begin{cases} r\sin\theta = a\sqrt{\left(\dfrac{1}{g_k(\omega)} - 1\right)(\xi_k^2 - 1)}\sqrt{1 - \eta_k^2}, \\ r\cos\theta = a\sqrt{1 - g_k(\omega)}\xi_k\eta_k, \end{cases} \tag{64}$$

where $k = 1, 2$ and

$$g_k(\omega) = \frac{a^2}{c^2}\frac{\varepsilon_z^{(k)}(\omega)}{\varepsilon_{\perp}^{(k)}(\omega)}. \tag{65}$$

The range of the spheroidal coordinate η_k is $-1 \le \eta_k \le 1$. Depending on the value of the function (65), the spheroidal coordinate ξ_k can have the following range:

$$\begin{array}{lll} 0 < \xi_k < 1 & \text{if} & g_k(\omega) < 0 \\ \xi_k > 1 & \text{if} & 0 < g_k(\omega) < 1 \\ i\xi_k > 0 & \text{if} & g_k(\omega) > 1 \end{array} \tag{66}$$

According to Eq. (64), the QD surface $r = a$ is defined in the spheroidal coordinates as

$$\begin{cases} \xi_k = \xi_k^{(0)} \equiv 1/\sqrt{1 - g_k(\omega)}, \\ \eta_k = \cos\theta. \end{cases} \tag{67}$$

Therefore, the part of the phonon potential $V_1(\mathbf{r})$ defined by Eq. (62) and the part of the phonon potential $V_2(\mathbf{r})$ defined by Eq. (63) coincide at the QD surface. Thus, the first boundary condition, given by Eq. (59), is satisfied.

Now, let us find the normal component of the displacement vector $\mathbf{D}$ at the QD surface. According to Eq. (61),

$$D_k(a, \theta, \phi) = \varepsilon_\perp^{(k)}(\omega) \left[(g_k(\omega)\cos^2\theta + \sin^2\theta) \left.\frac{\partial V_k}{\partial r}\right|_{r=a} + \frac{1 - g_k(\omega)}{a} \sin\theta\cos\theta \left.\frac{\partial V_k}{\partial \theta}\right|_{r=a} \right]. \tag{68}$$

Using relation (64) between the coordinates (ξ_k, η_k) and (r, θ), we can calculate each of the two partial derivatives from Eq. (68):

$$\left.\frac{\partial V_k}{\partial r}\right|_{r=a} = \frac{1}{a(g_k(\omega)\cos^2\theta + \sin^2\theta)} \left[\frac{g_k(\omega)}{\sqrt{1 - g_k(\omega)}} \left.\frac{\partial V_k}{\partial \xi_k}\right|_{\substack{\xi_k = \xi_k^{(0)} \\ \eta_k = \cos\theta}} + \cos\theta\sin^2\theta(1 - g_k(\omega)) \left.\frac{\partial V_k}{\partial \eta_k}\right|_{\substack{\xi_k = \xi_k^{(0)} \\ \eta_k = \cos\theta}} \right] \tag{69}$$

$$\left.\frac{\partial V_k}{\partial \theta}\right|_{r=a} = -\sin\theta \left.\frac{\partial V_k}{\partial \eta_k}\right|_{\substack{\xi_k = \xi_k^{(0)} \\ \eta_k = \cos\theta}}. \tag{70}$$

Substituting Eqs. (69) and (70) into Eq. (68), one obtains a simple formula:

$$D_k(a, \theta, \phi) = \frac{\varepsilon_\perp^{(k)}(\omega) g_k(\omega)}{a\sqrt{1 - g_k(\omega)}} \left.\frac{\partial V_k}{\partial \xi_k}\right|_{\substack{\xi_k = \xi_k^{(0)} \\ \eta_k = \cos\theta}}. \tag{71}$$

Finally, using the explicit form of the phonon potentials (62) and (63) as well as Eqs. (65) and (67), one can rewrite Eq. (71) as

$$D_1(a, \theta, \phi) = \frac{a}{c^2} \frac{\varepsilon_z^{(1)}(\omega)}{\sqrt{1 - g_1(\omega)}} \left.\frac{d\ln P_l^m(\xi_1)}{d\xi_1}\right|_{\xi_1 = \xi_1^{(0)}} P_l^m(\cos\theta) e^{im\phi}, \tag{72}$$

$$D_2(a, \theta, \phi) = \frac{a}{c^2} \frac{\varepsilon_z^{(2)}(\omega)}{\sqrt{1 - g_2(\omega)}} \left.\frac{d\ln Q_l^m(\xi_2)}{d\xi_2}\right|_{\xi_2 = \xi_2^{(0)}} P_l^m(\cos\theta) e^{im\phi}. \tag{73}$$

Substituting Eqs. (72) and (73) into the second boundary condition (60), one can see that it is satisfied only when the following equality is true

$$\varepsilon_z^{(1)}(\omega) \left(\xi \frac{d\ln P_l^m(\xi)}{d\xi} \right) \Big|_{\xi = 1/\sqrt{1 - g_1(\omega)}} = \varepsilon_z^{(2)}(\omega) \left(\xi \frac{d\ln Q_l^m(\xi)}{d\xi} \right) \Big|_{\xi = 1/\sqrt{1 - g_2(\omega)}}. \tag{74}$$

Thus, we have found the equation that defines the spectrum of polar optical phonons in a WZ spheroidal QD embedded in a WZ crystal. Note that Eq. (74) can be also obtained using a completely different technique developed by us for WZ nanocrystals of arbitrary shape [54]. It should be pointed out, that for a spheroidal QD with ZB crystal structure $\varepsilon_\perp^{(k)}(\omega) = \varepsilon_z^{(k)}(\omega) \equiv \varepsilon^{(k)}(\omega)$ and Eq. (74) reduces to the one obtained in Refs. [49, 50]. The fact that the spectrum of polar optical phonons does not depend on the absolute size of a QD [48, 49] is also seen from Eq. (74).

The case of a freestanding QD is no less important for practical applications. In this case the dielectric tensor of the exterior medium is a constant $\varepsilon_D \equiv \varepsilon_z^{(2)}(\omega) = \varepsilon_\perp^{(2)}(\omega)$. Therefore,

using the explicit form of associated Legendre polynomials P_l^m and omitting the upper index "(1)" in the components of the dielectric tensor of the QD, we can represent Eq. (74) in the following convenient form:

$$\sum_{n=0}^{\lfloor l-|m|/2\rfloor}\left[\frac{c^2}{a^2}\frac{\varepsilon_\perp(\omega)}{\varepsilon_D}|m|+\frac{\varepsilon_z(\omega)}{\varepsilon_D}(l-|m|-2n)-f_l^{|m|}\left(\frac{a}{c}\right)\right] \times\binom{l-|m|}{2n}\frac{(2n-1)!!\,(2l-2n-1)!!}{(2l-1)!!}\left[\frac{a^2}{c^2}\frac{\varepsilon_z(\omega)}{\varepsilon_\perp(\omega)}-1\right]^n=0, \tag{75}$$

where

$$f_l^m(\alpha)=\xi\left.\frac{d\ln Q_l^m(\xi)}{d\xi}\right|_{\xi=1/\sqrt{1-\alpha^2}}. \tag{76}$$

It can be shown that the function $f_l^m(\alpha)$ increases monotonely from $-\infty$ to 0 when α increases from 0 to ∞. As seen from Eq. (75), there are no phonon modes with $l=0$ and all phonon frequencies with $m\neq 0$ are twice degenerate with respect to the sign of m. For a spherical ($\alpha=1$) freestanding QD one has to take the limit $\xi\to\infty$ in Eq. (76), what results in $f_l^m(1)=-(l+1)$. Thus, in the case of a ZB spherical QD [$\varepsilon_\perp(\omega)=\varepsilon_z(\omega)\equiv\varepsilon(\omega)$; $a=c$], Eq. (75) gives the well-known equation $\varepsilon(\omega)/\varepsilon_D=-1-1/l$ derived in Ref. [48].

3.3.2. Freestanding ZnO Quantum Dots

In this Section we consider freestanding spheroidal ZnO QDs and examine the phonon modes with quantum numbers $l=1,2,3,4$ and $m=0,1$. The components of the dielectric tensor of WZ ZnO are given by Eq. (51). The exterior medium is considered to be air with $\varepsilon_D=1$. Figure 23(a) shows the spectrum of polar optical phonons with $m=0$ and Fig. 23(b) shows the spectrum of polar optical phonons with $m=1$. The frequencies with even l are plotted with solid curves while the frequencies with odd l are plotted with dashed curves. The frequencies in Fig. 23 are found as solutions of Eq. (75) and are plotted as a function of the ratio of the spheroidal semi-axes a and c. Thus, in the leftmost part of the plots we have the phonon spectrum for a spheroid degenerated into a vertical line segment; father to the right we have the spectrum for prolate spheroids; in the central part of the plots we have the phonon spectrum for a sphere; farther on we have the spectrum for oblate spheroids; and in the rightmost part of the plots we have the phonon spectrum for a spheroid degenerated into a horizontal flat disk.

The calculated spectrum of phonons in the freestanding ZnO QDs can be divided into three regions: confined TO phonons ($\omega_{z,\mathrm{TO}}<\omega<\omega_{\perp,\mathrm{TO}}$), interface phonons ($\omega_{\perp,\mathrm{TO}}<\omega<$

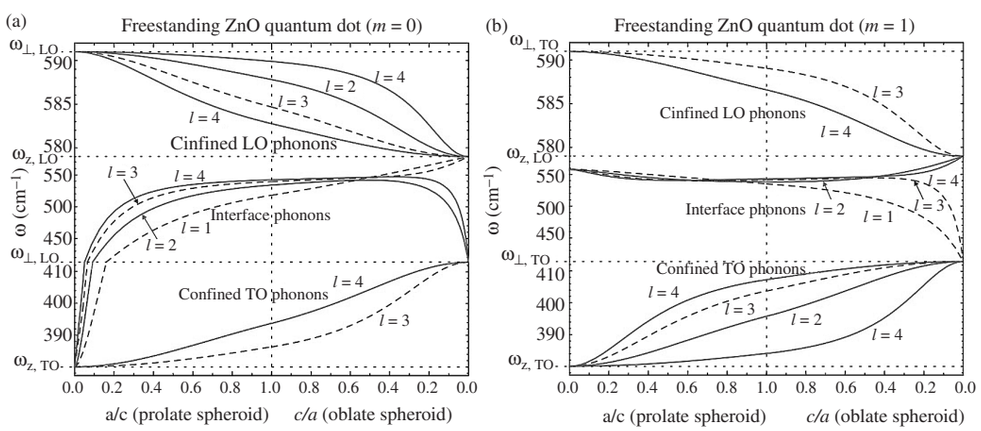

Figure 23. Frequencies of polar optical phonons with $l=1,2,3,4$ and $m=0$ (a) or $m=1$ (b) for a freestanding spheroidal ZnO QD as a function of the ratio of spheroidal semi-axes. Solid curves correspond to phonons with even l and dashed curves correspond to phonons with odd l. Frequency scale is different for confined TO, interface, and confined LO phonons.

$\omega_{z,\mathrm{LO}}$), and confined LO phonons ($\omega_{z,\mathrm{LO}} < \omega < \omega_{\perp,\mathrm{LO}}$). The above division into confined and interface phonons is based on the sign of the function $g(\omega)$ [see Eq. (65)]. We call the phonons with eigenfrequency ω interface phonons if $g(\omega) > 0$ and confined phonons if $g(\omega) < 0$. To justify the classification of phonon modes as interface and confined ones based on the sign of the function $g_1(\omega)$, let us consider the phonon potential (62) inside the QD. If $g_1(\omega) < 0$ then, according to Eq. (66), $0 < \xi_1 < 1$; therefore $P_l^m(\xi_1)$ is an oscillatory function of ξ_1 and the phonon potential (62) is mainly confined inside the QD. On the contrary, if $g_1(\omega) > 0$ then, according to Eq. (66), $\xi_1 > 1$ or $\mathrm{i}\xi_1 > 0$; therefore $P_l^m(\xi_1)$ increases monotonely with ξ_1 as ξ_1^l reaching the maximum at the QD surface together with the phonon potential (62). Note that vertical frequency scale in Fig. 23 is different for confined TO, interface, and confined LO phonons. The true scale is shown in Fig. 22.

Analyzing Eq. (75), one can find that for each pair (l, m) there is one interface optical phonon and $l - |m|$ confined optical phonons for $m \neq 0$ ($l - 1$ for $m = 0$). Therefore, we can see four interface phonons and six confined phonons for both $m = 0$ and $m = 1$ in Fig. 23. However, one can see that there are four confined LO phonons with $m = 0$ and only two confined LO phonons with $m = 1$. On the contrary, there are only two confined TO phonons with $m = 0$ and four confined TO phonons with $m = 1$ in Fig. 23.

When the shape of the spheroidal QD changes from the vertical line segment to the horizontal flat disk, the frequencies of all confined LO phonons decrease from $\omega_{\perp,\mathrm{LO}}$ to $\omega_{z,\mathrm{LO}}$. At the same time the frequencies of all confined TO phonons increase from $\omega_{z,\mathrm{TO}}$ to $\omega_{\perp,\mathrm{TO}}$. It is also seen from Fig. 23 that for very small ratios a/c, what is the case of so-called quantum rods, the interface phonons with $m = 0$ become confined TO phonons, while the frequencies of all interface phonons with $m = 1$ degenerate into a single frequency. When the shape of the spheroidal QD changes from the vertical line segment to the horizontal flat disk, the frequencies of interface phonons with odd l and $m = 0$ increase from $\omega_{z,\mathrm{TO}}$ to $\omega_{z,\mathrm{LO}}$, while the frequencies of interface phonons with even l and $m = 0$ increase for prolate spheroids starting from $\omega_{z,\mathrm{TO}}$, like for the phonons with odd l, but they farther decrease up to $\omega_{\perp,\mathrm{TO}}$ for oblate spheroids. On the contrary, when the shape of the spheroidal QD changes from the vertical line segment to the horizontal flat disk, the frequencies of interface phonons with odd l and $m = 1$ decrease from a single interface frequency to $\omega_{\perp,\mathrm{TO}}$, while the frequencies of interface phonons with even l and $m = 1$ decrease for prolate spheroids starting from a single frequency, like for the phonons with odd l, but they farther increase up to $\omega_{z,\mathrm{LO}}$ for oblate spheroids.

In the rest of this Section we study phonon potentials corresponding to the polar optical phonon modes with $l = 1, 2, 3, 4$ and $m = 0$. In Fig. 24 we present the phonon potentials for a spherical freestanding ZnO QD. The phonon potentials for QDs with arbitrary spheroidal shapes can be found analogously using Eqs. (62), (63) and the coordinate transformation (54). As seen from Fig. 24, the confined LO phonons are, indeed, confined inside the QD. However, unlike confined phonons in ZB QDs, confined phonons in WZ QDs slightly penetrate into the exterior medium. Potential of interface phonon modes is, indeed, localized near the surface of the WZ QD. While there are no confined TO phonons in ZB QDs, they appear in WZ QDs. It is seen from Fig. 24 that confined TO phonons are, indeed, localized mainly inside the QD. However, they penetrate into the exterior medium much stronger than confined LO phonons.

Figure 25 shows the calculated spectrum of polar optical phonons with $l = 1, 2, 3, 4$ and $m = 0$ in a spherical WZ ZnO QD as a function of the optical dielectric constant of the exterior mediumε_D. It is seen from Fig. 25 that the frequencies of interface optical phonons decrease substantially when ε_D changes from the vacuum's value ($\varepsilon_D = 1$) to the ZnO nanocrystal's value ($\varepsilon_D = 3.7$). At the same time the frequencies of confined optical phonons decrease only slightly with ε_D.

Using the theory of excitonic states in WZ QDs developed in this chapter, it can be shown that the dominant component of the wave function of the exciton ground state in spheroidal ZnO QDs is symmetric with respect to the rotations around the z-axis or reflection in the xy-plane. Therefore, the selection rules for the polar optical phonon modes observed in the resonant Raman spectra of ZnO QDs are $m = 0$ and $l = 2, 4, 6, \ldots$ The phonon modes with higher symmetry (smaller quantum number l) are more likely to be observed in the Raman

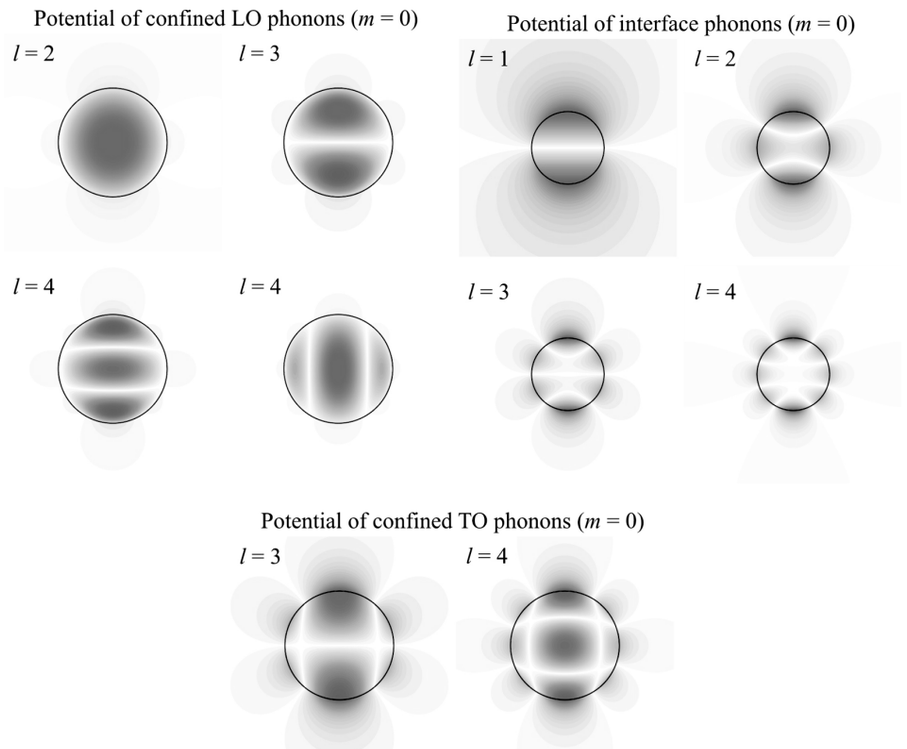

Figure 24. Cross-sections of phonon potentials corresponding to polar optical phonon modes with $l = 1, 2, 3, 4$ and $m = 0$ for the freestanding spherical ZnO QD. Z-axis is directed vertically. Black circle represents the QD surface. Reprinted with permission from [58], V. A. Fonoberov and A. A. Balandin, *J. Phys.: Cond. Matt.* 17, 1085 (2005). © 2005, IOP Publishing Ltd.

spectra. It is seen from Fig. 24, that the confined LO phonon mode with $l = 2$, $m = 0$ and the confined TO mode with $l = 4$, $m = 0$ are the confined modes with the highest symmetry among the confined LO and TO phonon modes, correspondingly. Therefore, they should give the main contribution to the resonant Raman spectrum of spheroidal ZnO QDs.

In fact, the above conclusion has an experimental confirmation. In the resonant Raman spectrum of spherical ZnO QDs with diameter 8.5 nm from Ref. 60], the main Raman peak in the region of LO phonons has the frequency 588 cm^{-1} and the main Raman peak in the region of TO phonons has the frequency 393 cm^{-1} (see large dots in Fig. 25). In accordance with Fig. 25, our calculations give the frequency 587.8 cm^{-1} of the confined LO phonon mode with $l = 2$, $m = 0$ and the frequency 393.7 cm^{-1} of the confined TO phonon mode with $l = 4$, $m = 0$. This excellent agreement of the experimental and calculated frequencies allows one to predict the main peaks in the LO and TO regions of a Raman spectra of spheroidal ZnO QDs using the corresponding curves from Fig. 23.

3.3.3. ZnO/MgZnO Quantum Dots

It is illustrative to consider spheroidal ZnO QDs embedded into a $Mg_{0.2}Zn_{0.8}O$ crystal. The components of the dielectric tensors of WZ ZnO and $Mg_{0.2}Zn_{0.8}O$ are given by Eqs. (51) and (52), correspondingly. The relative position of optical phonon bands of WZ ZnO and $Mg_{0.2}Zn_{0.8}O$ is shown in Fig. 22. It is seen from Eq. (65) that $g_1(\omega) < 0$ inside the shaded region corresponding to ZnO in Fig. 22 and $g_2(\omega) < 0$ inside the shaded region corresponding to $Mg_{0.2}Zn_{0.8}O$. As it has been shown earlier, the frequency region where $g_1(\omega) < 0$ corresponds to confined phonons in a freestanding spheroidal ZnO QD. However, there can be no confined phonons in the host $Mg_{0.2}Zn_{0.8}O$ crystal. Indeed, there are no physical solutions of Eq. (74) when $g_2(\omega) < 0$. The solutions of Eq. (74) are nonphysical in this case, because the spheroidal coordinates (ξ_2, η_2) defined by Eq. (64) cannot cover the entire

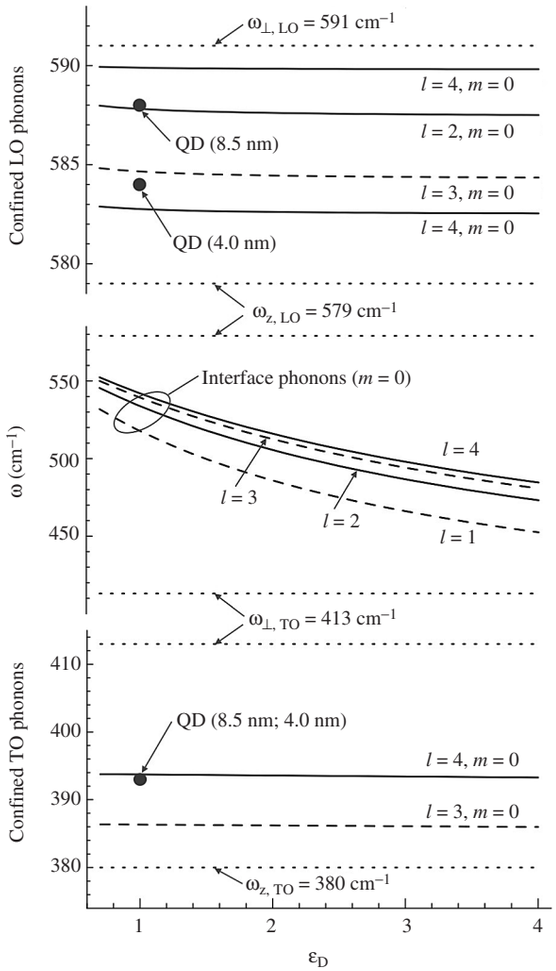

Figure 25. Spectrum of several polar optical phonon modes in spherical WZ ZnO nanocrystals as a function of the optical dielectric constant of the exterior medium. Note that the scale of frequencies is different for confined LO, interface, and confined TO phonons. Large black dots show the experimental points from Ref. [60]. Reprinted with permission from [54], V. A. Fonoberov and A. A. Balandin, *Phys. Rev. B* 70, 233205 (2004). © 2004, American Physical Society.

space outside the QD. If we allow the spheroidal coordinates (ξ_2, η_2) to be complex, then the phonon potential outside the QD becomes complex and diverges logarithmically when $\xi_2 = 1$; the latter is clearly nonphysical. It can be also shown that Eq. (74) does not have any solutions when $g_1(\omega) > 0$ and $g_2(\omega) > 0$. Therefore, the only case when Eq. (74) allows for physical solutions is $g_1(\omega) < 0$ and $g_2(\omega) > 0$. The frequency regions that satisfy the latter condition are cross-hatched in Fig. 22. There are two such regions: $\omega^{(1)}_{z,\mathrm{TO}} < \omega < \omega^{(2)}_{z,\mathrm{TO}}$ and $\omega^{(1)}_{z,\mathrm{LO}} < \omega < \omega^{(2)}_{z,\mathrm{LO}}$, which are further called the regions of TO and LO phonons, respectively.

Let us now examine the LO and TO phonon modes with quantum numbers $l = 1, 2, 3, 4$ and $m = 0, 1$. Figure 26(a) shows the spectrum of polar optical phonons with $m = 0$ and Fig. 26(b) shows the spectrum of polar optical phonons with $m = 1$. The frequencies with even l are plotted with solid curves while the frequencies with odd l are plotted with dashed curves. The frequencies in Fig. 26 are found as solutions of Eq. (74) and are plotted as a function of the ratio of the spheroidal semi-axes a and c, similarly to Fig. 23 for the freestanding spheroidal ZnO QD. Note that vertical frequency scale in Fig. 26 is different for TO phonons and LO phonons. The true scale is shown in Fig. 22.

Comparing Fig. 26(a) with Fig. 23(a) and Fig. 26(b) with Fig. 23(b) we can see the similarities and distinctions in the phonon spectra of the ZnO QD embedded into the $Mg_{0.2}Zn_{0.8}O$

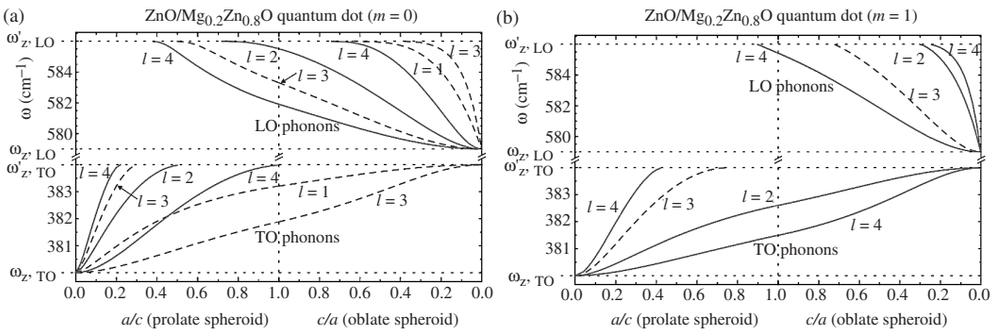

Figure 26. Frequencies of polar optical phonons with $l = 1, 2, 3, 4$ and $m = 0$ (a) or $m = 1$ (b) for a spheroidal $ZnO/Mg_{0.2}Zn_{0.8}O$ QD as a function of the ratio of spheroidal semi-axes. Solid curves correspond to phonons with even l and dashed curves correspond to phonons with odd l. Frequency scale is different for TO and LO phonons. Frequencies $\omega_{z,\mathrm{TO}}$ and $\omega_{z,\mathrm{LO}}$ correspond to ZnO and frequencies $\omega'_{z,\mathrm{TO}}$ and $\omega'_{z,\mathrm{LO}}$ correspond to $Mg_{0.2}Zn_{0.8}O$.

crystal and that of the freestanding ZnO QD. For a small ratio a/c we have the same number of TO phonon modes with the frequencies originating from $\omega^{(1)}_{z,\mathrm{TO}}$ for the embedded and freestanding ZnO QDs. With the increase of the ratio a/c the frequencies of TO phonons increase for both embedded and freestanding ZnO QDs, but the number of TO phonon modes gradually decreases in the embedded ZnO QD. When $a/c \to \infty$ there are only two phonon modes with odd l are left for $m = 0$ and two phonon modes with even l are left for $m = 1$. The frequencies of these phonon modes increase up to $\omega^{(2)}_{z,\mathrm{TO}}$ when $a/c \to \infty$. However, for this small ratio c/a we have the same number of LO phonon modes with the frequencies originating from $\omega^{(1)}_{z,\mathrm{LO}}$ for the embedded and freestanding ZnO QDs. With the increase of the ratio c/a the frequencies of all LO phonons increase for the embedded ZnO QD and the number of such phonons gradually decreases. When $c/a \to \infty$ there are no phonons left for the embedded ZnO QD. At the same time for the freestanding ZnO QD, with the increase of the ratio c/a the frequencies of two LO phonons with odd l and $m = 0$ and two LO phonons with even l and $m = 1$ decrease and go into the region of interface phonons.

It is seen from the previous paragraph that for the ZnO QD with a small ratio c/a embedded into the $Mg_{0.2}Zn_{0.8}O$ crystal the two LO and two TO phonon modes with odd l and $m = 0$ and with even l and $m = 1$ may correspond to interface phonons. To check this hypothesis, we further study phonon potentials corresponding to the polar optical phonon modes with $l = 1, 2, 3, 4$ and $m = 0$. In Fig. 27 we present the phonon potentials for the spheroidal ZnO QD with the ratio $c/a = 1/4$ embedded into the $Mg_{0.2}Zn_{0.8}O$ crystal. The considered ratio $c/a = 1/4$ of the spheroidal semi-axes is a reasonable value for epitaxial ZnO/ $Mg_{0.2}Zn_{0.8}O$ QDs. It is seen in Fig. 27 that the LO phonon with $l = 1$, one of the LO phonons with $l = 3$, and all two TO phonons are, indeed, interface phonons, since they achieve their maximal and minimal values at the surface of the ZnO QD. It is interesting that the potential of interface TO phonons is strongly extended along the z-axis, while the potential of interface LO phonons is extended in the xy-plane. All other LO phonons in Fig. 27 are confined. The most symmetrical phonon mode is, again, the one with $l = 2$ and $m = 0$. Therefore, it should give the main contribution to the Raman spectrum of oblate spheroidal ZnO QDs embedded into the $Mg_{0.2}Zn_{0.8}O$ crystal. Unlike for freestanding ZnO QDs, no pronounced TO phonon peaks are expected for the embedded ZnO QDs.

3.4. Raman Spectroscopy of ZnO Quantum Dots

Both resonant and non-resonant Raman scattering spectra have been measured for ZnO nanostructures such as thin films [61, 62], nanowires [63, 64], nanotubes [65], and nanoparticles [25, 60, 66]. Due to the WZ crystal structure of bulk ZnO, the frequencies of both LO and TO phonons are split into two frequencies with symmetries A_1 and E_1. In ZnO, in addition to LO and TO phonon modes, there are two non-polar Raman active phonon modes with symmetry E_2. The low-frequency E_2 mode is associated with the vibration of the

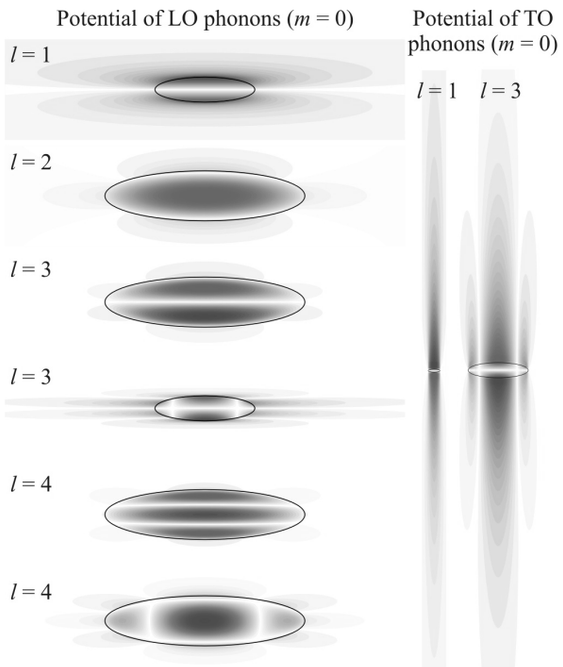

Figure 27. Cross-sections of phonon potentials corresponding to polar optical phonon modes with $l = 1, 2, 3, 4$ and $m = 0$ for the oblate spheroidal ZnO/$Mg_{0.2}Zn_{0.8}O$ QD with aspect ratio 1/4. Z-axis is directed vertically. Black ellipse represents the QD surface. Reprinted with permission from [58], V. A. Fonoberov and A. A. Balandin, *J. Phys.: Cond. Matt.* 17, 1085 (2005). © 2005, IOP Publishing Ltd.

heavy Zn sublattice, while the high frequency E_2 mode involves only the oxygen atoms. The above phonon modes are clearly identified in the Raman scattering spectra of bulk ZnO [67, 68]. The Raman spectra of ZnO nanostructures always show shift of the bulk phonon frequencies [25, 60, 61–66]. The origin of this shift, its strength, and dependence on the QD diameter are still the subjects of debates. Understanding the nature of the observed shift is important for interpretation of the Raman spectra and understanding properties of ZnO nanostructures.

In this Section of the chapter, we present data that clarify the origin of the peak shift. There are three main mechanisms that can induce phonon peak shifts in ZnO nanostructures: (i) spatial confinement within the dot boundaries; (ii) phonon localization by defects (oxygen deficiency, zinc excess, surface impurities, etc.); or (iii) laser-induced heating in nanostructure ensembles. Usually, only the first mechanism, referred to as optical phonon confinement, is invoked as an explanation of the phonon frequency shifts in ZnO nanostructures [60].

The optical phonon confinement has been originally introduced to explain the observed frequency shift in small covalent semiconductor nanocrystals. It attributes the red shift and broadening of the Raman peaks to the relaxation of the phonon wave vector selection rule due to the finite size of the nanocrystals [69]. It has been recently shown theoretically by us [54, 58] that while this phenomenological model is justified for small covalent nanocrystals, it cannot be applied to ionic ZnO QDs with the sizes larger than 4 nm. The latter is due to the fact that the polar optical phonons in ZnO are almost non-dispersive in the region of small wave vectors. In addition, the asymmetry of the WZ crystal lattice leads to the QD shape-dependent splitting of the frequencies of polar optical phonons in a series of discrete frequencies. Here we argue that all three aforementioned mechanisms contribute to the observed peak shift in ZnO nanostructures, and that in many cases, the contribution of the optical phonon confinement can be relatively small compared to other mechanisms.

We carried out systematic non-resonant and resonant Raman spectroscopy of ZnO QDs with diameter of 20 nm together with the bulk reference sample. The experimental Raman

spectroscopy data for ZnO QDs presented in this Section is mostly taken from study reported by Alim, Fonoberov, and Balandin [70]. To elucidate the effects of heating we varied the excitation laser power over a wide range. The reference WZ bulk ZnO crystal (University Wafers) had dimensions $5 \times 5 \times 0.5$ mm^3 with a-plane (11–20) facet. The investigated ZnO QDs have been produced by the wet chemistry method. The dots had nearly spherical shape of the average diameter of 20 nm, and good crystalline structure as evidenced by the TEM study. The purity of ZnO QDs in a powder form was 99.5%. A Renishaw micro-Raman spectrometer 2000 with visible (488 nm) and UV (325 nm) excitation lasers was employed to measure the non-resonant and resonant Raman spectra of ZnO, correspondingly. The number of gratings in the Raman spectrometer was 1800 for visible laser and 3000 for UV laser. All spectra were taken in the backscattering configuration.

The non-resonant and resonant Raman spectra of bulk ZnO crystal and ZnO QD sample are shown in Figs. 28 and 29, respectively. A compilation of the reported frequencies of Raman active phonon modes in bulk ZnO gives the phonon frequencies 102 cm^{-1}, 379 cm^{-1}, 410 cm^{-1}, 439 cm^{-1}, 574 cm^{-1}, and 591 cm^{-1} for the phonon modes E_2 (low), A_1 (TO), E_1 (TO), E_2 (high), A_1 (LO), and $E1$ (LO), correspondingly [70]. In our spectrum from the bulk ZnO, the peak at 439 cm^{-1} corresponds to E_2 (high) phonon, while the peaks at 410 cm^{-1} and 379 cm^{-1} correspond to E_1 (TO) and A_1 (TO) phonons, respectively. No LO phonon peaks are seen in the spectrum of bulk ZnO. On the contrary, no TO phonon peaks are seen in the Raman spectrum of ZnO QDs. In the QD spectrum, the LO phonon peak at 582 cm^{-1} has a frequency intermediate between those of A_1 (LO) and E_1 (LO) phonons, which is in agreement with theoretical calculations [54, 58]. The broad peak at about 330 cm^{-1} seen in both spectra in Fig. 28 is attributed to the second-order Raman processes.

The E_2 (high) peak in the spectrum of ZnO QDs is red shifted by 3 cm^{-1} from its position in the bulk ZnO spectrum (see Fig. 28). Since the diameter of the examined ZnO QDs is relatively large, such pronounced redshift of the E_2 (high) phonon peak can hardly be attributed only to the optical phonon confinement by the QD boundaries. Measuring the anti-Stokes spectrum and using the relationship between the temperature T and the relative intensity of Stokes and anti-Stokes peaks $I_S/I_{AS} \approx \exp[\hbar\omega/k_BT]$, we have estimated the temperature of the ZnO QD powder under visible excitation to be below 50 °C. Thus, heating in the non-resonant Raman spectra cannot be responsible for the observed frequency shift. Therefore, we conclude that the shift of E_2 (high) phonon mode is due to the presence of intrinsic defects in the ZnO QD samples, which have about 0.5% of impurities. This conclusion is supported by a recent study [71] that showed a strong dependence of the E_2 (high) peak on the isotopic composition of ZnO.

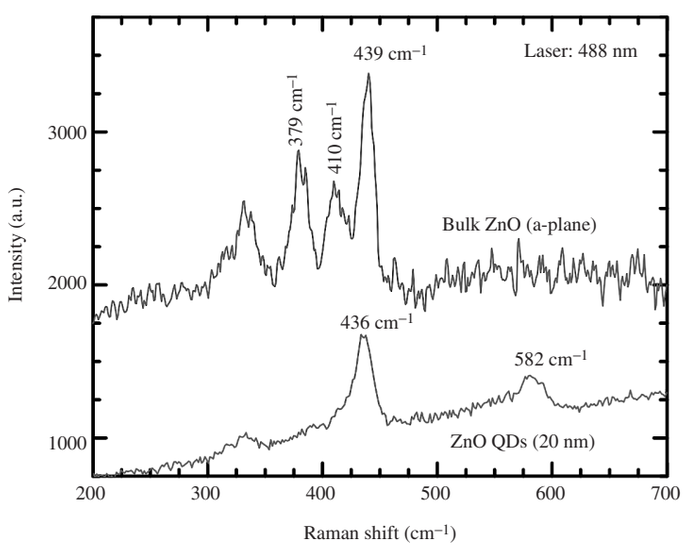

Figure 28. Non-resonant Raman scattering spectra of bulk ZnO (a-plane) and ZnO QDs (20 nm in diameter). Laser power is 15 mW. Linear background is subtracted for the bulk ZnO spectrum.

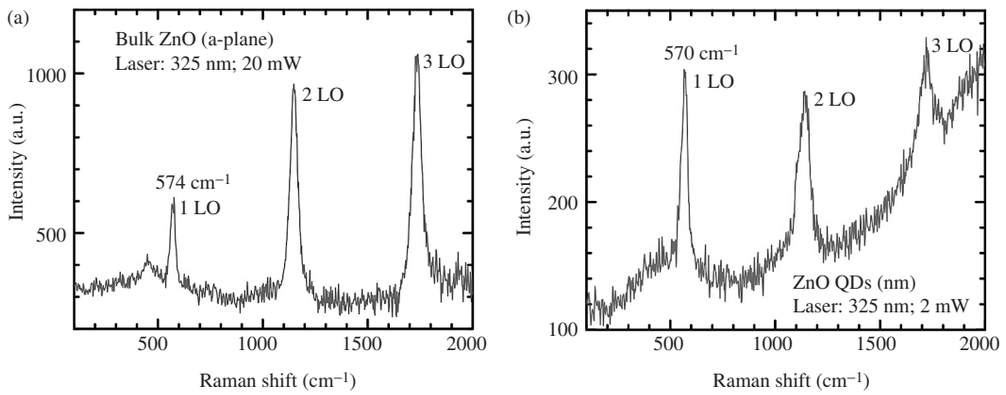

Figure 29. Resonant Raman scattering spectra of (a) a-plane bulk ZnO and (b) ZnO QDs. Laser power is 20 mW for bulk ZnO and 2 mW for ZnO QDs. PL background is subtracted from the bulk ZnO spectrum.

Figure 29(a)–(b) show the measured resonant Raman scattering spectra of bulk ZnO and ZnO QDs, respectively. A number of LO multi-phonon peaks are observed in both resonant Raman spectra. The frequency 574 cm^{-1} of 1LO phonon peak in bulk ZnO corresponds to A_1 (LO) phonon, which can be observed only in the configuration when the *c*-axis of WZ ZnO is parallel to the sample face. When the *c*-axis is perpendicular to the sample face, the E_1 (LO) phonon is observed, instead [67]. According to the theory of polar optical phonons in WZ nanocrystals [54, 58], the frequency of 1LO phonon mode in ZnO QDs should be between 574 and 591 cm^{-1}. However, Fig. 29(b) shows that this frequency is only 570 cm^{-1}. The observed redshift of the 1LO peak in the powder of ZnO QDs is too large to be caused by the intrinsic defects or impurities. The only possible explanation of the observed redshift is a local temperature raise induced by UV laser in the powder of ZnO QDs [72]. To check this assumption, we varied the UV laser power as well as the area of the illuminated spot on the ZnO QD powder sample.

Figure 30 shows the LO phonon frequency in the powder of ZnO QDs as a function of UV laser power for two different areas of the illuminated spot. It is seen from Fig. 30, that for the illuminated 11 μm^2 spot, the redshift of the LO peak increases almost linearly with UV

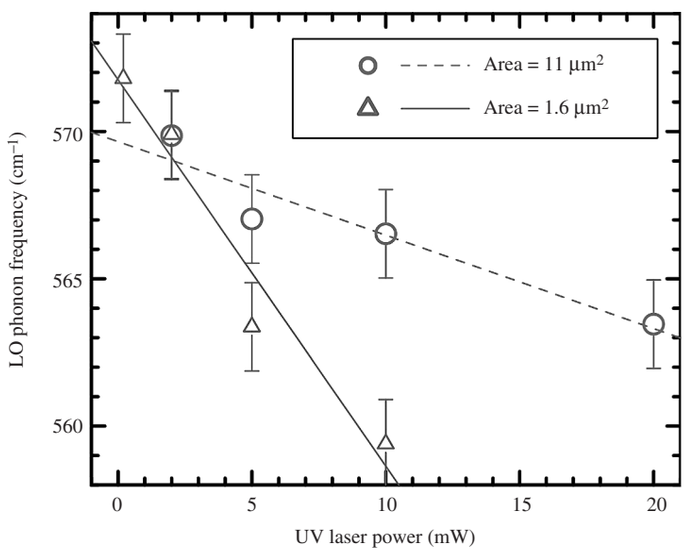

Figure 30. LO phonon frequency shift in ZnO QDs as a function of the excitation laser power. Laser wavelength is 325 nm. Circles and triangles correspond to the illuminated sample areas of 11 μm^2 and 1.6 μm^2. Reprinted with permission from [70], K. A. Alim, V. A. Fonoberov, and A. A. Balandin, *Appl. Phys. Lett.* 86, 053103 (2005). © 2005, American Institute of Physics.

laser power and reaches about 7 cm^{-1} for the excitation laser power of 20 mW. As expected, by reducing the area of the illuminated spot to 1.6 μm^2, we get a faster increase of the LO peak redshift with the laser power. In the latter case, the LO peak redshift reaches about 14 cm^{-1} for laser power of only 10 mW. An attempt to measure the LO phonon frequency using the illuminated spot of area 1.6 μm^2 and UV laser power 20 mW resulted in the destruction of the ZnO QDs on the illuminated spot, which was confirmed by the absence of any ZnO signature peaks in the measured spectra at any laser power.

It is known that the melting point of ZnO powders is substantially lower than that of a ZnO crystal (~2000 °C), what results in the ZnO powder evaporation at temperature less than 1400 °C [73]. The density of the examined ensemble of ZnO QDs is only about 8% of the density of ZnO crystal, what means that there is large amount of air between the QDs and, therefore, very small thermal conductivity of the illuminated spot. This explains the origin of such strong excitation laser heating effect on the Raman spectra of ZnO QDs.

If the temperature rise in our sample is proportional to the UV laser power, then the observed 14 cm^{-1} LO phonon redshift should correspond to a temperature rise around 700 °C at the sample spot of area 1.6 μm^2 illuminated by the UV laser with power 10 mW. In this case the increase of the laser power to 20 mW would lead to the temperature of about 1400 °C and the observed destruction of the QD sample spot. To verify this conclusion we have calculated the LO phonon frequency of ZnO as a function of temperature. Taking into account the thermal expansion and anharmonic coupling effects, the LO phonon frequency can be written as [74]

$$\omega(T) = \exp\left[-\gamma \int_0^T \{2\alpha_\perp(T') + \alpha_\parallel(T')\} dT'\right](\omega_0 - M_1 - M_2) + M_1\left[1 + \frac{2}{e^{\hbar\omega_0/2k_BT} - 1}\right] + M_2\left[1 + \frac{3}{e^{\hbar\omega_0/3k_BT} - 1} + \frac{3}{(e^{\hbar\omega_0/3k_BT} - 1)^2}\right], \quad (77)$$

where the Grüneisen parameter of the LO phonon in ZnO $\gamma = 1.4$ [75], the thermal expansion coefficients $\alpha_\perp(T)$ and $\alpha_\parallel(T)$ for ZnO are taken from Ref. [76], and the anharmonicity parameters M_1 and M_2 are assumed to be equal to those of the A_1 (LO) phonon of GaN [74]: $M_1 = -4.14$ cm^{-1} and $M_2 = -0.08$ cm^{-1}. By fitting of the experimental data shown in Fig. 30 (area = 1.6 μm^2) with Eq. (1), the LO phonon frequency at $T = 0$ K, ω_0, was found to be 577 cm^{-1}. At the same time, it followed from Eq. (1) that the observed 14 cm^{-1} redshift shown in Fig. 30, indeed, corresponded to ZnO heated to the temperature of about 700 °C.

In summary, we have clarified the origin of the phonon peak shifts in ZnO QDs. By using non-resonant and resonant Raman spectroscopy, we have determined that there are three factors contributing to the observed peak shifts. They are the optical phonon confinement by the QD boundaries, the phonon localization by defects or impurities, and the laser-induced heating in nanostructure ensembles. While the first two factors were found to result in phonon peak shifts of few cm^{-1}, the third factor, laser-induced heating, could result in the resonant Raman peak redshift as large as tens of cm^{-1}.

4. CONCLUSIONS

In this chapter we have given a detail theoretical description of the excitonic and phonon properties of GaN and ZnO QDs. Whenever available experimental data was provided for comparison with theoretical and modeling results. The chapter serves as a reference source for information on the electron, hole, exciton states, and radiative decay times for WZ and ZB GaN/AlN, WZ GaN/$Al_{0.15}Ga_{0.85}N$ and WZ ZnO QDs. The multi-band model description detailed in this chapter has yielded excitonic energies and radiative decay times, which agree very well with available experimental data for all considered QDs. It has been demonstrated that a strong piezoelectric field characteristic for WZ GaN/AlN QDs can be used as an additional tuning parameter for the optical response of such nanostructures.

A particular attention in this chapter has been given to exciton states in colloidal ZnO QDs in the intermediate quantum confinement regime. The considered regime corresponds

to the QD sizes, which are slightly larger than the size of an exciton in bulk ZnO. The presented results and proposed analytical approximation for the radiative lifetime can be used for interpretation of experimental data. The small radiative lifetime and rather thick dead layer in ZnO QDs are expected to be beneficial for optoelectronic device applications due to improved luminescence and exciton separation from the surface defects. We have reviewed the arguments, which state that depending on the fabrication technique and ZnO QD surface quality, the origin of UV PL in ZnO QDs is either recombination of confined excitons or surface-bound ionized acceptor–exciton complexes.

The chapter outlines analytical derivation for the interface and confined polar optical phonon modes in spheroidal QDs with WZ crystal structure. The presented theory has been applied to study phonon frequencies and potentials as a function of the ratio of spheroidal semi-axes for freestanding spheroidal ZnO QDs and spheroidal ZnO QDs embedded into the $Mg_{0.2}Zn_{0.8}O$ crystal. Similarly to the case of the spheroidal QDs with ZB crystal structure, a discrete spectrum of frequencies has been obtained for the *interface* polar optical phonons in WZ spheroidal QDs. At the same time, the discrete spectrum of frequencies has been also found for *confined* polar optical phonons in WZ QDs, while the confined polar optical phonons in ZB QDs have a single frequency (LO). The positions of polar optical phonon lines observed in the resonant Raman spectra of spherical WZ ZnO QDs have been explained quantitatively. The model described in this chapter allows one to explain and accurately predict phonon peaks in the Raman spectra not only for WZ ZnO nanocrystals, nanorods, and epitaxial $ZnO/Mg_{0.2}Zn_{0.8}O$ QDs, but also for any WZ spheroidal QD either freestanding or embedded into another crystal.

Finally, the chapter presents considerations, which clarify the origin of the phonon frequency shifts in ZnO QDs. The described results shed new light on the controversial issue of the interpretation of Raman spectra of ZnO and other nanostructures. The methods outlined in this chapter can be used to identify peaks in the Raman scattering spectra from ZnO nanostructures.

ACKNOWLEDGMENT

The research on GaN and ZnO quantum dots conducted in the Nano-Device Laboratory (http://ndl.ee.ucr.edu/) has been supported, in part, by the National Science Foundation (NSF) and the US Civilian Research and Development Foundation (CRDF) through the grants to A.A.B. The authors thank NDL member Khan Alim for providing experimental data on Raman spectroscopy of ZnO quantum dots. The authors acknowledge useful discussions with Prof. E. P. Pokatilov (Moldova State University) on properties of GaN quantum dots.

REFERENCES

1. F. Widmann, B. Daudin, G. Feuillet, Y. Samson, J. L. Rouviere, and N. Pelekanos, *J. Appl. Phys.* 83, 7618 (1998).
2. F. Widmann, J. Simon, B. Daudin, G. Feuillet, J. L. Rouviere, N. T. Pelekanos, and G. Fishman, *Phys. Rev. B* 58, R15989 (1998).
3. P. Ramval, S. Tanaka, S. Nomura, P. Riblet, and Y. Aoyagi, *Appl. Phys. Lett.* 73, 1104 (1998).
4. P. Ramval, P. Riblet, S. Nomura, Y. Aoyagi, and S. Tanaka, *J. Appl. Phys.* 87, 3883 (2000).
5. V. J. Leppert, C. J. Zhang, H. W. H. Lee, I. M. Kennedy, and S. H. Risbud, *Appl. Phys. Lett.* 72, 3035 (1998).
6. E. Borsella, M. A. Garcia, G. Mattei, C. Maurizio, P. Mazzoldi, E. Cattaruzza, F. Gonella, G. Battagin, A. Quaranta, and F. D'Acapito, *J. Appl. Phys.* 90, 4467 (2001).
7. E. Martinez-Guerrero, C. Adelmann, F. Chabuel, J. Simon, N. T. Pelekanos, G. Mula, B. Daudin, G. Feuillet, and H. Mariette, *Appl. Phys. Lett.* 77, 809 (2000).
8. B. Daudin, G. Feuillet, H. Mariette, G. Mula, N. Pelekanos, E. Molva, J. L. Rouviere, C. Adelmann, E. Martinez-Guerrero, J. Barjon, F. Chabuel, B. Bataillou, and J. Simon, *Jpn. J. Appl. Phys.* 40, 1892 (2001).
9. A. D. Andreev and E. P. O'Reilly, *Phys. Rev. B* 62, 15851 (2000).
10. V. A. Fonoberov, E. P. Pokatilov, and A. A. Balandin, *J. Nanosci. Nanotechnol.* 3, 253 (2003); V. A. Fonoberov and A. A. Balandin, *J. Appl. Phys.* 94, 7178 (2003); V. A. Fonoberov and A. A. Balandin, *J. Vac. Sci. Technol. B* 22, 2190 (2004).
11. L. D. Landau and E. M. Lifshitz, Eds., "Theory of Elasticity," 3rd Edition. Pergamon, Oxford, 1986.
12. I. P. Ipatova, V. G. Malyshkin, and V. A. Shchukin, *J. Appl. Phys.* 74, 7198 (1993).

13. E. P. Pokatilov, V. A. Fonoberov, V. M. Fomin, and J. T. Devreese, *Phys. Rev. B* 64, 245328 (2001).
14. F. Mireles and S. E. Ulloa, *Phys. Rev. B* 62, 2562 (2000).
15. C. Pryor, M. E. Pistol, and L. Samuelson, *Phys. Rev. B* 56, 10404 (1997).
16. V. A. Fonoberov, E. P. Pokatilov, and A. A. Balandin, *Phys. Rev. B* 66, 085310 (2002).
17. G. W. Hooft, W. A. Poel, L. W. Molenkamp, and C. T. Foxon, *Phys. Rev. B* 35, 8281 (1987).
18. L. S. Dang, G. Fishman, H. Mariette, C. Adelmann, E. Martinez, J. Simon, B. Daudin, E. Monroy, N. Pelekanos, J. L. Rouviere, and Y. H. Cho, *J. Kor. Phys. Soc.* 42, S657 (2003); J. Simon, N. T. Pelekanos, C. Adelmann, E. Martinez-Guerrero, R. Andre, B. Daudin, Le Si Dang, and H. Mariette, *Phys. Rev. B* 68, 035312 (2003).
19. A. P. Alivisatos, *Science* 271, 933 (1996).
20. L. Guo, S. Yang, C. Yang, P. Yu, J. Wang, W. Ge, and G. K. L. Wong, *Appl. Phys. Lett.* 76, 2901 (2000).
21. D. W. Bahnemann, C. Kormann, and M. R. Hoffmann, *J. Phys. Chem.* 91, 3789 (1987).
22. E. A. Muelenkamp, *J. Phys. Chem. B* 102, 5566 (1998).
23. A. Wood, M. Giersig, M. Hilgendorff, A. Vilas-Campos, L. M. Liz-Marzan, and P. Mulvaney, *Aust. J. Chem.* 56, 1051 (2003).
24. E. M. Wong and P. C. Searson, *Appl. Phys. Lett.* 74, 2939 (1999).
25. H. Zhou, H. Alves, D. M. Hofmann, W. Kriegseis, B. K. Meyer, G. Kaczmarczyk, and A. Hoffmann, *Appl. Phys. Lett.* 80, 210 (2002).
26. A. Dijken, E. A. Muelenkamp, D. Vanmaekelbergh, and A. Meijerink, *J. Phys. Chem. B* 104, 1715 (2000).
27. R. Viswanatha, S. Sapra, B. Satpati, P. V. Satyam, B. N. Dev, and D. D. Sarma, *J. Mater. Chem.* 14, 661 (2004).
28. L. Brus, *J. Phys. Chem.* 90, 2555 (1986).
29. L. E. Brus, *J. Chem. Phys.* 80, 4403 (1984).
30. M. Califano, A. Zunger, and A. Franceschetti, *Nanoletters* 4, 525 (2004).
31. V. A. Fonoberov, E. P. Pokatilov, V. M. Fomin, and J. T. Devreese, *Phys. Rev. Lett.* 92, 127402 (2004).
32. A. Mews, A. V. Kadavanich, U. Banin, and A. P. Alivisatos, *Phys. Rev. B* 53, R13242 (1996).
33. V. A. Fonoberov and A. A. Balandin, *Phys. Rev. B* 70, 195410 (2004).
34. The following parameters of WZ ZnO are taken from Ref. [36]: electron effective mass $m_e = 0.24$; Rashba-Sheka-Pikus parameters of the valence band $A_1 = -3.78$, $A_2 = -0.44$, $A_3 = 3.45$, $A_4 = -1.63$, $A_5 = -1.68$, $A_6 = -2.23$, $A_7 = 0.47$ nm^{-1}; crystal-field splitting energy $\Delta_{cr} = 38$ meV; and dielectric constant $\varepsilon = 3.7$. The band-gap energy of WZ ZnO is $E_g = 3.437$eV [37]. The heavy-hole effective mass can be estimated as $m_{hh} \approx 1/|A_2| = 2.27$, what gives the ratio $m_{hh}/m_e = 9.5$ in agreement with the tight-binding calculations [43]. Using the reduced exciton mass $\mu = m_e m_{hh}/(m_e + m_{hh})$, the exciton Bohr radius is estimated to be $a_B = 4\pi\varepsilon_0\hbar^2\varepsilon/e^2 m_0\mu = 0.90$ nm.
35. Y. Kayanuma, *Phys. Rev. B* 38, 9797 (1988).
36. W. R. L. Lambrecht, A. V. Rodina, S. Limpijumnong, B. Segall, and B. K. Meyer, *Phys. Rev. B* 65, 075207 (2002).
37. D. C. Reynolds, D. C. Look, B. Jogai, C. W. Litton, G. Cantwell, and W. C. Harsch, *Phys. Rev. B* 60, 2340 (1999).
38. P. Lawaetz, *Phys. Rev. B* 4, 3460 (1971).
39. S. I. Pekar, *Sov. Phys. JETP* 6, 785 (1958).
40. M. Combescot, R. Combescot, and B. Roulet, *Eur. Phys. J. B* 23, 139 (2001).
41. D. C. Reynolds, D. C. Look, B. Jogai, J. E. Hoelscher, R. E. Sherriff, M. T. Harris, and M. J. Callahan, *J. Appl. Phys.* 88, 2152 (2000).
42. E. I. Rashba and G. E. Gurgenishvili, *Sov. Phys. Solid State* 4, 759 (1962).
43. A. Kobayashi, O. F. Sankey, S. M. Volz, and J. D. Dow, *Phys. Rev. B* 28, 935 (1983).
44. S. Mahamuni, K. Borgohain, B. S. Bendre, V. J. Leppert, and S. H. Risbud, *J. Appl. Phys.* 85, 2861 (1999).
45. L. W. Wang and A. Zunger, *Phys. Rev. B* 53, 9579 (1996).
46. L. W. Wang, *J. Phys. Chem. B* 105, 2360 (2001).
47. V. A. Fonoberov and A. A. Balandin, *Appl. Phys. Lett.* 85, 5971 (2004).
48. R. Englman and R. Ruppin, *Phys. Rev. Lett.* 16, 898 (1966). R. Englman and R. Ruppin, *J. Phys. C* 1, 614 (1968).
49. P. A. Knipp and T. L. Reinecke, *Phys. Rev. B* 46, 10310 (1992).
50. F. Comas, G. Trallero-Giner, N. Studart, and G. E. Marques, *Phys. Rev. B* 65, 073303 (2002). F. Comas, G. Trallero-Giner, N. Studart, and G. E. Marques, *J. Phys.: Condens. Matter* 14, 6469 (2002).
51. S. N. Klimin, E. P. Pokatilov, and V. M. Fomin, *Phys. Stat. Sol. B* 184, 373 (1994).
52. E. P. Pokatilov, S. N. Klimin, V. M. Fomin, J. T. Devreese, and F. W. Wise, *Phys. Rev. B* 65, 075316 (2002).
53. D. Romanov, V. Mitin, and M. Stroscio, *Physica B* 316/317, 359 (2002); D. Romanov, V. Mitin, and M. Stroscio, *Physica E* 12, 491 (2002); D. A. Romanov, V. V. Mitin, and M. A. Stroscio, *Phys. Rev. B* 66, 115321 (2002).
54. V. A. Fonoberov and A. A. Balandin, *Phys. Rev. B* 70, 233205 (2004).
55. M. A. Stroscio and M. Dutta, "Phonons in Nanostructures." Cambridge University Press, Cambridge, 2001.
56. C. Chen, M. Dutta, and M. A. Stroscio, *J. Appl. Phys.* 95, 2540 (2004); C. Chen, M. Dutta, and M. A. Stroscio, *Phys. Rev. B* 70, 075316 (2004); C. Chen, M. Dutta, and M. A. Stroscio, *J. Appl. Phys.* 96, 2049 (2004).
57. C. A. Arguello, D. L. Rousseau, and S. P. S. Porto, *Phys. Rev.* 181, 1351 (1969).
58. V. A. Fonoberov and A. A. Balandin, *J. Phys.: Condens. Matt.* 17, 1085 (2005).
59. C. Bundesmann, M. Schubert, D. Spemann, T. Butz, M. Lorenz, E. M. Kaidashev, M. Grundmann, N. Ashkenov, H. Neumann, and G. Wagner, *Appl. Phys. Lett.* 81, 2376 (2002).
60. M. Rajalakshmi, A. K. Arora, B. S. Bendre, and S. Mahamuni, *J. Appl. Phys.* 87, 2445 (2000).
61. X. T. Zhang, Y. C. Liu, Z. Z. Zhi, J. Y. Zhang, Y. M. Lu, D. Z. Shen, W. Xu, G. Z. Zhong, X. M. Fan, and X. G. Kong, *J. Phys. D: Appl. Phys.* 34, 3430 (2001).

62. C. Bundesmann, N. Ashkenov, M. Schubert, D. Spemann, T. Butz, E. M. Kaidashev, M. Lorenz, and M. Grundmann, *Appl. Phys. Lett.* 83, 1974 (2003).
63. H. T. Ng, B. Chen, J. Li, J. Han, M. Meyyappan, J. Wu, S. X. Li, and E. E. Haller, *Appl. Phys. Lett.* 82, 2023 (2003).
64. X. Wang, Q. Li, Z. Liu, J. Zhang, Z. Liu, and R. Wang, *Appl. Phys. Lett.* 84, 4941 (2004).
65. Y. J. Xing, Z. H. Xi, Z. Q. Xue, X. D. Zhang, J. H. Song, R. M. Wang, J. Xu, Y. Song, S. L. Zhang, and D. P. Yu, *Appl. Phys. Lett.* 83, 1689 (2003).
66. Z. Wang, H. Zhang, L. Zhang, J. Yuan, S. Yan, and C. Wang, *Nanotechnology* 14, 11 (2003).
67. N. Ashkenov, B. N. Mbenkum, C. Bundesmann, V. Riede, M. Lorenz, D. Spemann, E. M. Kaidashev, A. Kasic, M. Schubert, M. Grundmann, G. Wagner, H. Neumann, V. Darakchieva, H. Arwin, and B. Monemar, *J. Appl. Phys.* 93, 126 (2003).
68. J. F. Scott, *Phys. Rev. B* 2, 1209 (1970).
69. H. Richter, Z. P. Wang, and L. Ley, *Solid State Commun.* 39, 625 (1981).
70. K. A. Alim, V. A. Fonoberov, and A. A. Balandin, *Appl. Phys. Lett.* 86, 053103 (2005).
71. J. Serrano, F. J. Manjon, A. H. Romero, F. Widulle, R. Lauck, and M. Cardona, *Phys. Rev. Lett.* 90, 055510 (2003).
72. L. Bergman, X. B. Chen, J. L. Morrison, J. Huso, and A. P. Purdy, *J. Appl. Phys.* 96, 675 (2004).
73. K. Park, J. S. Lee, M. Y. Sung, and S. Kim, *Jpn. J. Appl. Phys.* 41, 7317 (2002).
74. W. S. Li, Z. X. Shen, Z. C. Feng, and S. J. Chua, *J. Appl. Phys.* 87, 3332 (2000).
75. F. Decremps, J. Pellicer-Porres, A. M. Saitta, J. C. Chervin, and A. Polian, *Phys. Rev. B* 65, 092101 (2002).
76. H. Iwanaga, A. Kunishige, and S. Takeuchi, *J. Mater. Sci.* 35, 2451 (2000).